Geophysical Journal International

Geophys. J. Int. (2020) **221,** 981–1001
Advance Access publication 2020 January 29
GJI Marine geosciences and applied geophysics

doi: 10.1093/gji/ggaa052

Magmatism versus serpentinization—crustal structure along the 13°N segment at the Mid-Atlantic Ridge

C. Peirce,[1] A.H. Robinson,[1] M.J. Funnell,[1] R.C. Searle,[1] C.J. MacLeod[2] and T.J. Reston[3]

[1] *Department of Earth Sciences, Durham University, South Road, Durham DH13LE, UK. E-mail: christine.peirce@durham.ac.uk*
[2] *School of Earth and Ocean Sciences, Cardiff University, Park Place, Cardiff CF103AT, UK*
[3] *School of Geography, Earth and Environmental Sciences, University of Birmingham, Edgbaston, Birmingham B152TT, UK*

Accepted 2020 January 27. Received 2020 January 9; in original form 2019 August 8

SUMMARY

A region of oceanic core complexes (OCCs) exists at 13°N on the Mid-Atlantic Ridge that is regarded as a type site. This site includes two OCCs at 13°20′N and 13°30′N, thought to be in the active and dying stages of evolution, and two together called the Ashadze Complex (centred at 13°05′N) that are considered to be relict. Here we describe the results of *S*-wave seismic modelling along an ∼200-km-long 2-D transect traversing, south-to-north, through both the Mercurius and Marathon fracture zones, the southern outside corner of the 13°N segment, the OCCs, the ridge axis deviation in trend centred at 13°35′N, and the youngest oceanic crust of the eastern ridge flank to the north. Our inversion model, and the corresponding V_p/V_s ratio, show that the majority of the crust beneath the 13°30′N OCC comprises metamorphosed lithologies that have been exhumed to the shallowest subseabed level, while basaltic lithologies underlie the 13°20′N OCC. The transition between these contrasting crustal structures occurs over a distance of <5 km, and extends to at least ∼2 km depth below seafloor. The northern and southern OCCs of the Ashadze Complex have contrasting structures at shallow depth, with the northern OCC having a faster *S*-wave velocity in the upper crust. A V_p/V_s ratio of >1.9 (and equivalent Poisson's ratio of >0.3) indicates exhumed and/or metamorphosed lithologies beneath the bathymetric depression between them and within the crust beneath the southern OCC. Between the northern and southern flanks of the Marathon fracture zone and northern flank of Mercurius fracture zone, the lower crust has a relatively low V_p/V_s ratio suggesting that the deformation associated with Marathon fracture zone, which facilitates fluid ingress, extends laterally within the lower crust. Marathon fracture zone itself is underlain by a broad zone of low *S*-wave velocity (∼2.0 km s^{-1}) up to ∼20 km wide from the seabed to at least the mid-crust, that is mirrored in a high V_p/V_s ratio and lower density, particularly deeper than ∼1 km below seabed within its bathymetric footprint. Volcanic domains are highlighted by a low V_p/V_s ratio of <1.6 (and equivalent Poisson's ratio of <0.15). Our combined seismic and density models favour the localized model of OCC evolution. They also show a considerable ridge-parallel variability in the amount and distribution of magmatic versus metamorphosed crust. Our results suggest that the current focus of magmatism lies to the north of the 13°20′N OCC, where the magmatic accretion-type seabed morphology observed is mirrored in the pattern of microseismicity, suggesting that its inward-facing median-valley-wall fault may link to the 13°20′N OCC detachment surface. Magmatism and active faulting behind (to the west) the footwall breakaway of the 13°30′N OCC, and the microseismicity concentrated in a band along its southern flank, suggest a readjustment of ridge geometry along axis is underway. As part of this, a transform offset is forming that will ultimately accommodate the 13°30′N OCC in its inside corner on the eastern flank of the ridge axis to the north.

Key words: Controlled source seismology; Crustal imaging; Crustal structure; Mid-ocean ridge processes.

1 INTRODUCTION

Shallowing seafloor, high fluid and heat flow and seismicity mark mid-ocean ridge locations where new oceanic crust is created. Along their length, these ridges are broken up into individual segments by transform faults, which offset them laterally, juxtaposing younger against older lithosphere. Many of these fault systems can be traced to the continental margins as fracture zones, which represent their relic past. As the number of surveys of mid-ocean ridges increases, and in a broader range of ridge settings, it has become clear that crustal formation is not solely a magmatically driven process but, instead, includes a diversity of tectonic processes operating over a wide range of inter-related scales and time frames.

1.1 Detachments and oceanic core complexes

As the spreading rate drops, and plate separation fluctuates from being accommodated by magmatism to being primarily accommodated by faulting (e.g. Buck *et al.* 2005), the seafloor that forms at a mid-ocean ridge becomes rougher due to an increase in normal fault throw (e.g. Macdonald 1982). Not only is such a variation in spreading style observed on a segment scale over 10s of kilometres, it is also observed on a local scale linked to the waxing and waning of the magma supply to the segment, and the extent to which magma can flow laterally towards the segment ends (e.g. Shaw 1992; Sempéré *et al.* 1993; Howell *et al.* 2016). Such focusing results in the long-established crustal thickness proxy for volume of magma supply (e.g. Kuo & Forsyth 1988; Thibaud *et al.* 1998).

3-D numerical modelling of the controls on mid-ocean ridge fault topography and morphology (e.g. Howell *et al.* 2019) demonstrates an interplay between periods during which magmatism dominates and ridge-parallel inward-facing normal faults form, and periods during which faulting dominates as magma supply wanes, and detachments form. The end-member of fault-dominated seafloor morphology at slow spreading rates is a long-lived detachment (Cann *et al.* 1997; Tucholke *et al.* 1998). Analytical modelling of these systems demonstrates how the mechanical properties of the lithosphere control fault initiation and cessation (e.g. Forsyth 1992; Buck 1993; Lavier *et al.* 2000), and that the size and spacing of faults is dependent on the ratio, M, between magmatic intrusion and stretching (Buck *et al.* 2005).

When M approaches 1, magmatic spreading dominates and axis-bounding normal faults migrate rapidly away from the ridge axis neovolcanic zone. As they reach the colder, stronger lithosphere off-axis, fault slip ceases and a new fault forms on-axis at the start of a new cycle (Howell *et al.* 2019). As the magma supply drops, M decreases towards 0.5, and fault migration slows in response. Consequently, faults remain active for longer, developing greater throws, and they become more widely spaced across axis (Howell *et al.* 2019). Eventually, if $M = 0.5$ is reached, faults remain active until the magmatic conditions change (e.g. Buck *et al.* 2005; Tucholke *et al.* 2008; Howell *et al.* 2019). Howell *et al.*'s (2019) 3-D modelling further shows that if a long-lived detachment has formed, and if the magmatic conditions change adjacent to it, the short-lived normal faults typical of magmatic accretion then form and migrate off-axis. These faults may episodically link to the long-lived detachment at depth to form a slip plane that is laterally continuous along axis for a period of time. On this basis, Howell *et al.* (2019) postulate that the location, extent, and active/inactive state of a detachment is controlled by the temporal and lateral variation in magma supply along axis.

There is currently considerable debate on whether a single detachment extends along the entire length of a segment or whether it is a localized feature within a segment, with Reston & Ranero (2011) and Reston (2018) arguing that the full seafloor extent of detachments could be masked by rider blocks resulting from along axis variation in lithospheric strength. Consequently, two end-member models exist—Smith *et al.*'s (2006, 2008) segment-scale model and MacLeod *et al.*'s (2009) localized-scale model—in which the degree, frequency and focus of magma supply control, to a first order, the location of detachment initiation, its lifespan, the asymmetry between ridge flanks (e.g. Reston 2018) and the along axis extent or connectivity, together with the initiation and development of transform faults.

Cross-cutting the entire crust, seabed observations show that detachments first exhume a blocky massif crustal section and, ultimately, a domed and striated region of the footwall (known as an oceanic core complex—OCC), that comprises mantle rocks intruded by plutonic gabbros (e.g. Tucholke & Lin 1994; Cann *et al.* 1997; Tucholke *et al.* 1998; MacLeod *et al.* 2009; Sauter *et al.* 2013). Thus, a diverse assemblage of highly altered and deformed eruptive, plutonic and mantle-derived ultramafic rocks is exposed at the seabed (e.g. MacLeod *et al.* 2002; Escartin *et al.* 2003, 2017; Dick *et al.* 2008; Albers *et al.* 2019; Sanfilippo *et al.* 2019), suggesting not only a complex pattern of deformation, but also that significant fluid circulation occurs.

The mechanics of slip along detachment faults, how they accommodate spreading, and what controls their onset, orientation and geometry both across and along axis, are also the subject of much debate (e.g. Reston 2018 and references therein). Detachment fault surfaces emerge from beneath the seafloor (at what is known as the hanging-wall cut-off) at angles too low to be consistent with models of extensional faulting alone (Buck *et al.* 2005). However, such low angles may be explained by initiation along a deep, steeply dipping rupture surface that rolls over prior to seafloor exhumation (Buck 1988; MacLeod *et al.* 2009, 2011; Morris *et al.* 2009; Reston 2018).

Local earthquake studies reveal patterns in seismicity that appear to demarcate the detachment surface to depth (e.g. deMartin *et al.* 2007; Collins *et al.* 2012; Grevemeyer *et al.* 2013; Schlindwein & Schmid 2016; Parnell-Turner *et al.* 2017). Focal mechanisms of these events reveal both compression and extension events that are attributed to volume expansion resulting from serpentinization or magma chamber filling (e.g. Grevemeyer *et al.* 2013), and fault hinge roll-over extensional faulting extending beneath the crust (e.g. Parnell-Turner *et al.* 2017). Regardless of cause, the pattern of seismicity suggests that crustal formation is dominated by two modes of deformation which define OCC evolution, namely: (i) extension upon detachment initiation at depth and (ii) compression in the footwall as the OCC is subsequently exhumed at the seafloor. This stress state change in the footwall is consistent with kinematic models of detachment fault behaviour (e.g. Buck 1988) and observations of reverse faulting in detachment footwalls (e.g. Pressling *et al.* 2012), suggesting that this compressional faulting is more likely triggered by bending stresses rather than volume expansion.

Reston (2018) considers the tectonics of slow and ultraslow spreading systems, using the Mid-Atlantic Ridge (MAR) and Southwest Indian Ridge (SWIR) as examples; proposing a model in which both amagmatic and magmatic crustal formation may occur via a succession of detachment faults that accommodate magmatism in their footwall, undergo low-angle footwall roll-over on exhumation, expose lower crustal and upper mantle lithologies at the seabed within volcanic terranes, and result in both apparent symmetric and asymmetric spreading. Either side of the SWIR

spreading axis, regions of exhumed seafloor comprise a series of ridge-parallel elongate highs, with both inward- and outward-facing fault-formed flanks interpreted by Sauter *et al.* (2013) as reflecting a succession of detachment faults of alternating polarity (Reston & McDermott 2011).

Building on the MacLeod *et al.* (2009) model for individual localized OCCs, Reston & McDermott (2011) suggest that successive detachments could migrate across the rift axis, each to be cut by a new detachment, and if flexure of the exhuming footwall causes strain weakening, the polarity of successive faults may alternate. Reston (2018) explains such observations using a model of amagmatic crustal formation which contains a series of faults that initiate at a fixed, but deep-seated, rift axis located between the two diverging plates. Here the formation of a new detachment is controlled by rheology, and truncation of an existing detachment occurs when and where the footwall has been fractured and weakened by bending. Phases of magmatism, whether in the footwall or supplying the neovolcanic zone, act to extend the active lifespan of the detachment, such that it could continue laterally beneath rafted blocks of rougher volcanic terrane.

Reston's (2018) model is based primarily on observations from the SWIR, where wide-angle seismic data modelling suggests two modes of crustal formation in which a volcanic layer forms up to a few kilometres thick (Minshull *et al.* 2006), or where areas of smooth seafloor exhibit pervasive, downward-decreasing metamorphism to a depth of 6 km below seafloor (Momoh *et al.* 2017). A lack of observed Moho reflections (Minshull *et al.* 2006) suggests that instead of a crust–mantle boundary occurring as a distinct interface (at seismic wavelengths), there is instead a transitional region. It has also become clear that the definition of the crust (and thus origin of 'Moho' reflections) in such slow- and ultraslow-spreading settings is now challenged, since sections of the ridge axis are shown to comprise exhumed mantle at the seabed, located adjacent to the layered structure formed by magmatic accretion. Consequently, such reflections may originate at a distinct traditional crust–mantle interface or at a serpentinization front within the upper mantle. In this paper we therefore use the term crust to describe material above the change (interface or transition) to normal mantle, and Moho reflections to occur there.

At the SWIR, most microseismic activity is observed in a continuous along axis band, with maximum depths ranging from 20 ± 5 km beneath exhumed seafloor to ∼5 km depth in the vicinity of volcanic terranes. This has been attributed to the varying depth of the 700°C isotherm (Schlindwein & Schmid 2016) and delimits the extent of brittle faulting. The general lack of shallower seismicity beneath the exhumed terrane may result from serpentinization and hydration of the fractured mantle, enabled by the passage of water along faults (Reston & Pérez Gussinyé 2007), with Schlindwein & Schmid (2016) suggesting that the considerable thickness of the brittle layer results from cooling by extensive circulation of water. However, Grevemeyer *et al.* (2019) demonstrate that Schlindwein & Schmid's (2016) apparent lack of shallow seismicity and the observation of apparent deep-seated seismicity is, instead, a result of station corrections being applied that do not take account of the thin layer of low-velocity sediment present. When updated, the pattern of seismicity conforms to that expected for the global temperature-depth relationship.

1.2 Transform faults and fracture zones

The relationship between ridge axis segment ends and segment-bounding transform faults (TF) and fracture zones (FZ) is not well understood. Ridge-segment-offsetting TFs are characterized by valleys tens of kilometres wide, whose depth increases with increasing distance between adjacent ridge tips. The transform valley is thought to reflect the isostatic response of a thin underlying crust (White *et al.* 1984), while down-faulting may also play a role due to thermal contraction as plate spreading continues (Pockalny *et al.* 1996). Transverse ridges, composed of large quantities of serpentinized peridotite, are often captured on one side of the transform valley, suggesting that not only do these fault systems represent a significant fluid flow path to the deeper crust and upper mantle, but also that density driven buoyancy contributes to their shallower bathymetric depth (Bonatti 1976, 1978). Since normal seafloor fabric continues across these ridges, Pockalny *et al.* (1996) suggest that they form as a result of trans-tensional extension.

Although the shallow bathymetry of the ridge-transform-fracture zone inside corner is thought to be dynamically supported (e.g. Searle & Laughton 1977; Severinghaus & Macdonald 1988; Blackman & Forsyth 1991), the lithosphere of the outside corner is thought to be locked to that across the FZ, resulting in strong coupling between lithospheres of different ages (e.g. Tuzo Wilson 1965). OCC-like massifs have been observed in the inside corner high position (Reston *et al.* 2002), with similar features mirrored in the outside corner. As these massifs share matching patterns of corrugations on their surfaces, and are very similar in dimensions and morphological characteristics, they are thought to result from a ridge jump. The inside corner is, thus, dissected by propagation of the adjacent spreading axis, or by a new spreading axis forming as a non-transform ridge axis discontinuity evolves into either a transform offset or an overlapping spreading centre (Reston *et al.* 2002).

Lithological sampling and seismic imaging at TFs in the Atlantic and Pacific reveal variable rock characteristics that could be expected to influence faulting behaviour (Bonatti 1978; Tréhu & Purdy 1984; Calvert & Potts 1985; Detrick *et al.* 1993; van Avendonk *et al*. 1998, 2001). The transform fault is often characterized by an apparently thinned crust, accompanied by reduced seismic velocity over a broad zone that is attributed to alteration of the upper mantle, and uplift related to serpentinite buoyancy (e.g. Detrick & Purdy 1980; Detrick *et al.* 1982; White *et al.* 1984; Minshull *et al.* 1991; Detrick *et al.* 1993). Such low-velocity zones have been ascribed to intense fracturing and hydrothermal alteration associated with strike-slip motion along the active fault trace, that extends to the base of the crust (Roland *et al.* 2012 and references therein). If fluid pathways are open to the lower crust and upper mantle, alteration of lower crustal gabbros would produce amphibole, serpentine and talc, and serpentinization would result from alteration of the peridotites of the uppermost mantle. Serpentinites have been dredged from Atlantic FZs (e.g. Bonatti 1976, 1978) and Pacific TFs (e.g. Hébert *et al.* 1983; Cannat *et al.* 1990; Hekinian *et al.* 1992), and serpentine diapirs have been proposed as the origin of transverse ridge formation in the Vema FZ (Bonatti 1976, 1978). The presence of serpentine and talc within the fault zone is cited as one possible explanation for its primarily aseismic nature, due to their relatively low strength (e.g. Moore *et al.* 1997).

1.3 V_p/V_s and Poisson's ratios

Although a number of seismic studies of mid-ocean ridge crust have been undertaken over recent decades, few have included the

analysis of *S*-waves as well as *P*-waves. Early studies where *S*-wave velocity structure has been determined include Fowler (1976) at the flanks of the MAR, and Bratt & Solomon (1984) for the East Pacific Rise (EPR). More recently at the EPR, *S*-wave structure has been defined using traveltime inversion, forward waveform modelling, and reflectivity analysis of expanded spread profiles (Vera *et al.* 1990), together with amplitude modelling of data acquired with both source and receiver located close to the seafloor (Christeson *et al.* 1994). Full waveform inversion of reflected and refracted arrivals has also been undertaken to resolve both the *P*- and *S*-wave velocity structure of the upper crust (e.g. Christeson *et al.* 1997; Collier & Singh 1998).

Recording *S*-waves is far more challenging than *P*-waves, being dependent both on the generation of *S*-waves themselves, by *P*-to-*S*-wave conversion somewhere along the subseabed propagation path, and the need for good coupling between the seabed and the sensor. Given the lack of sediment cover in near-ridge environments and the rough topography of slow-spreading ridges, which also degrades lateral phase coherence between shots (Spudich & Orcutt 1980), achieving good seabed-sensor coupling is difficult. Furthermore, the location of *S*-wave arrivals, within or behind the *P*-wave wave train, and the general level of background noise also affect the ability to identify arrival onset and, thus, pick arrival traveltimes to a degree of accuracy suitable for forward or inverse modelling.

Where co-located *P*-wave (V_p) and *S*-wave (V_s) velocity–depth models are available, V_p/V_s or Poisson's ratios can be calculated. The value of these ratios can subsequently be used:

(i) as a discriminator of composition (e.g. Domenico 1984; Christensen & Mooney 1995; Christensen 1996),
(ii) as a proxy for magma-rich vs magma-poor crustal formation (e.g. Grevemeyer *et al.* 2018a),
(iii) as a locator of accumulated melt within magma systems (e.g. Walsh 1968, 1969; Taylor & Singh 2002),
(iv) to locate regions of hydration (e.g. Grevemeyer *et al.* 2018b),
(v) to determine the nature of cracking (e.g. Hudson 1980; Berge *et al.* 1992; Collier & Singh 1998; Carlson 2010, 2014), and
(vi) to evaluate the extent of porosity and permeability (amongst other characteristics such as temperature) that facilitate hydrothermal fluid circulation (e.g. Kim *et al.* 2018).

Based on their contrasting velocity gradients, Grevemeyer *et al.* (2018a) argue that *P*-wave velocity can be used to discriminate between magmatically formed oceanic crust and serpentinized mantle that has been exhumed to shallow crustal level. However, this approach does not readily lend itself to distinguishing between crust resulting from different types of formation process. Instead, they propose that (in their fig. 4), as serpentinites are characterized by a V_p/V_s ratio of $\geq$1.9 instead of the 1.75–1.85 for basalts and gabbros of the oceanic crust (e.g. Christensen 1996, 2004; Carlson & Miller 1997, 2004), this is a better proxy to distinguish regions of serpentinized mantle (e.g. Bullock & Minshull 2005; Prada *et al.* 2016), the extent of fluid flow to the lower crust and uppermost mantle (e.g. Grevemeyer *et al.* 2018b), and the degree of lower crust and uppermost mantle exhumation that occurs at the slowest spreading rates (e.g. Peirce *et al.* 2019b).

Consequently, V_p/V_s or Poisson's ratios are variously both used to investigate lithology, and in particular the extent of serpentinized mantle when considered in a local OCC tectonic and geological context. Although equivalent, we include both in this paper to enable direct comparison to previous studies.

1.4 This study

Along the 13°N segment of the MAR, a number of OCCs are observed that are considered to span a range of evolutionary stages, from currently active through to dying and relict (Fig. 1a). Furthermore, this segment of the MAR, bounded to the south by the Marathon and Mercurius FZ-TFs, makes it an ideal system for studying both the processes involved in OCC formation and their relation to the evolution of the wider ridge segment. To investigate the subsurface structure and lithology of OCCs of the 13°N segment and the bounding TF-FZ system to the south, three research expeditions were undertaken on the RRS James Cook between 2014 and 2016:

(i) JC102 & JC109–Peirce (2014a, 2014b)—which undertook a passive ocean-bottom seismograph deployment and recovery to study local microseismicity. The results of this passive imaging have been reported by Parnell-Turner *et al.* (2017) and the pattern of microseismicity observed between JC102 and JC109 is shown in Fig. 2(a), and
(ii) JC132–Reston & Peirce (2016)—which undertook active-source seismic (wide-angle refraction and multichannel reflection), shipboard gravity, magnetic, and swath bathymetry data acquisition, together with autonomous underwater vehicle near-seabed swath bathymetry and magnetic surveying. The combined shipboard and near-seabed magnetics were reported by Searle *et al.* (2016), and their detailed analysis is discussed in Searle *et al.* (2018).

Here we describe the results of modelling *S*-wave traveltimes along an ~200-km-long 2-D transect acquired during JC132 (hereafter Profile R; Fig. 1). The results of *P*-wave seismic and gravity modelling along Profile R are reported by Peirce *et al.* (2019a). This 2-D profile also traversed the 3-D tomographic seismic grid acquired over the 13°20′N and 13°30′N OCCs (henceforth referred to as the 1320 and 1330 OCCs; Fig. 1a) during the same expedition, to specifically determine their internal structure and the geometry of the detachment surface. The results of the 3-D tomography-based modelling have been reported by Simão *et al.* (2016), and will be published elsewhere (Simão *et al.* 2020 forthcoming).

2 GEOLOGICAL SETTING

A region of OCCs exists at 13°N on the western flank of the MAR, that is regarded as a type site (e.g. MacLeod *et al.* 2002; Escartin *et al.* 2003, 2008, 2017). This region includes: the 1320 and 1330 OCCs (Fig. 1) that are thought to be in the active and dying stages of evolution respectively; two further OCCs, together called the Ashadze Complex (centred at 13°05′N) that are considered to be relict (e.g. Cherkashov *et al.* 2008); and a number of OCCs fossilised in the bathymetry off-axis. Higher resolution (~4 m) swath bathymetry imaging of the OCCs (Figs 1c and 2), achieved by multiple passes at a range of azimuths, clearly shows the geometry of each detachment's breakaway (seabed footwall cut-off of the detachment) and hanging-wall cut-off, and the inward-facing normal fault structures of the intervening seabed.

The 1320 and 1330 OCCs have widths of ~7 km and ~12 km along axis respectively, and are ~5.5 km and ~8 km in length in the direction of spreading. Assuming a consistent half-rate of 12 km Myr^{-1} and symmetrical spreading, extension along the detachment associated with each may, therefore, have been on-going for ~0.5 Myr and ~0.7 Myr. Near-bottom sonar imagery suggests that the 1320 detachment may still be active (Escartin *et al.* 2017). In contrast, the 1330 OCC is surrounded by volcanic craters, and displays an apparent termination of the detachment fault and observed

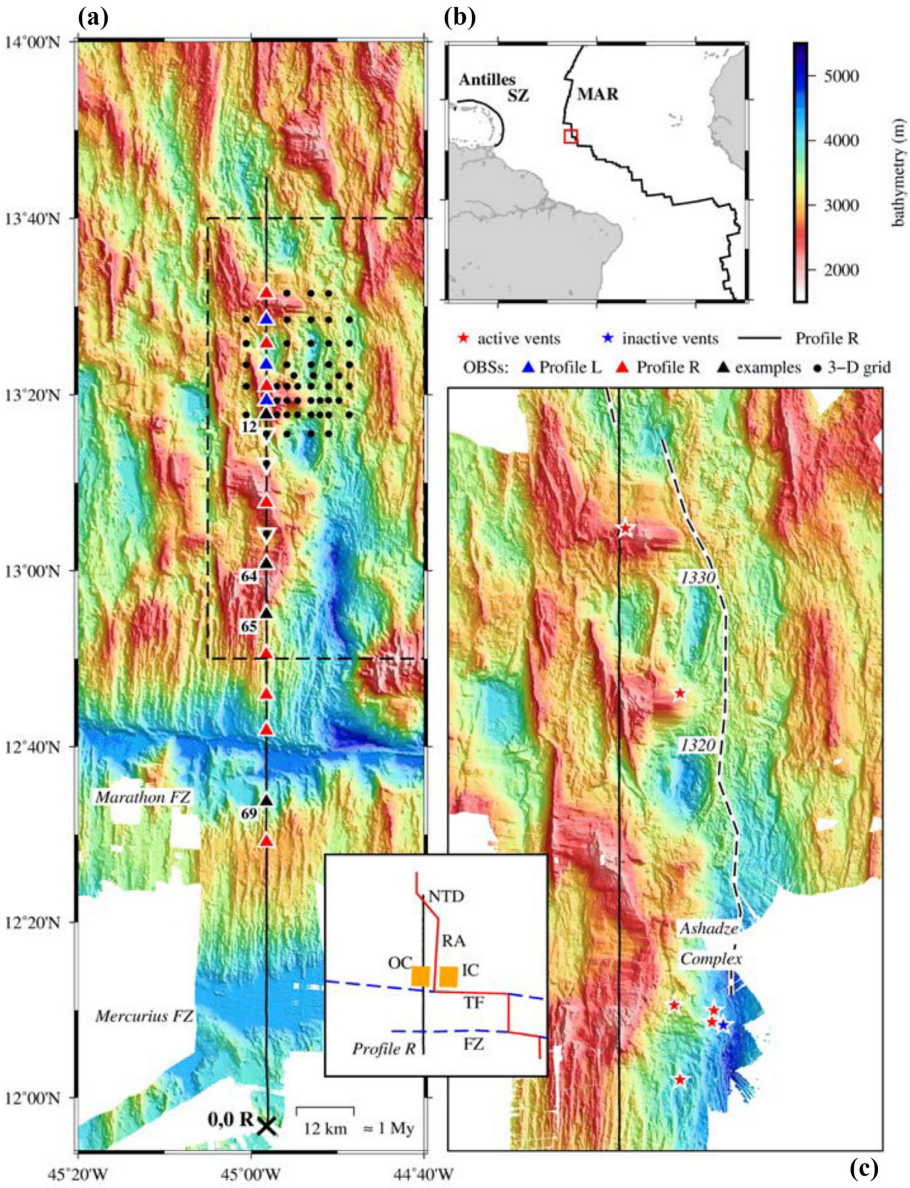

Figure 1. Bathymetry of the 13°N region of the Mid-Atlantic Ridge. (a) Location of Profile R (solid black line) and the OBSs of this study (triangles with white outlines), together with its intersection with a 3-D grid of OBSs (black dots) also deployed during JC132 (Simão *et al.* 2016 and forthcoming Simão *et al.* 2020). OBSs marked by blue-filled triangles only recorded shots fired along a co-incident profile acquired as part of the 3-D grid and were recovered prior to shooting Profile R, while numbered, black-filled triangles show OBSs for which example record sections are shown in Figs 3–5 or whose location is referred to in the text. Inverted unfilled triangles mark OBSs that did not record *S*-waves. Marathon and Mercurius FZ locations are labelled. Inset shows a schematic of the current ridge-transform geometry (red) and nomenclature adopted. RA—ridge axis; NTD—non-transform discontinuity; IC—inside corner and OC—outside corner (orange regions); TF—transform fault; FZ—fracture zone (blue dashed lines); SZ—subduction zone (*cf.* b). Long-dashed box shows the location of (c). (b) Location of the study area (red box) in the central Atlantic. (c) Profile R showing its crossing of each OCC, together with the location of active (red stars) and inactive (blue stars) hydrothermal vents (Beltenev *et al.* 2007; Cherkashov *et al.* 2010a,b, 2013, 2016; Pertsev *et al.* 2012; Bortnikov *et al.* 2015). Mallows & Searle's (2012) average ridge axis is marked by the black-dashed line.

propagation of adjacent volcanic ridges into it, thus suggesting it to be either in its final life stage or recently inactive (MacLeod *et al.* 2009; Mallows & Searle 2012).

A wide range of lithologies including gabbros, peridotites, basalts, and deformed fault rocks and mass-wasted rubble have been sampled at, or at shallow depth beneath, the seabed (MacLeod *et al.* 2009; Pertsev *et al.* 2009; Escartin *et al.* 2017), similar to those observed from the OCCs of the 15°20′N (Albers *et al.* 2019) and 16°30′N (Sanfilippo *et al.* 2019) areas of the MAR. Geochemical analysis of the basalts recovered from the 13°N region reveals a change in magmatic activity from a magma-poor phase at the initiation of detachment faulting, to an apparently more magma-rich phase at the present time (Wilson *et al.* 2013). Several active and extinct hydrothermal fields have been found within the 13°N segment, including on the exposed 1320 and 1330 detachment surfaces (Fig. 1; Beltenev *et al.* 2007; Cherkashov *et al.* 2010b; Pertsev *et al.* 2012, 2013; Bortnikov *et al.* 2015, 2016). The 1330 vents have been dated at up to ∼100 kyr in age and show no apparent age correlation with distance off-axis. Older deposits are found near the axis and active sites more than 5 km off-axis

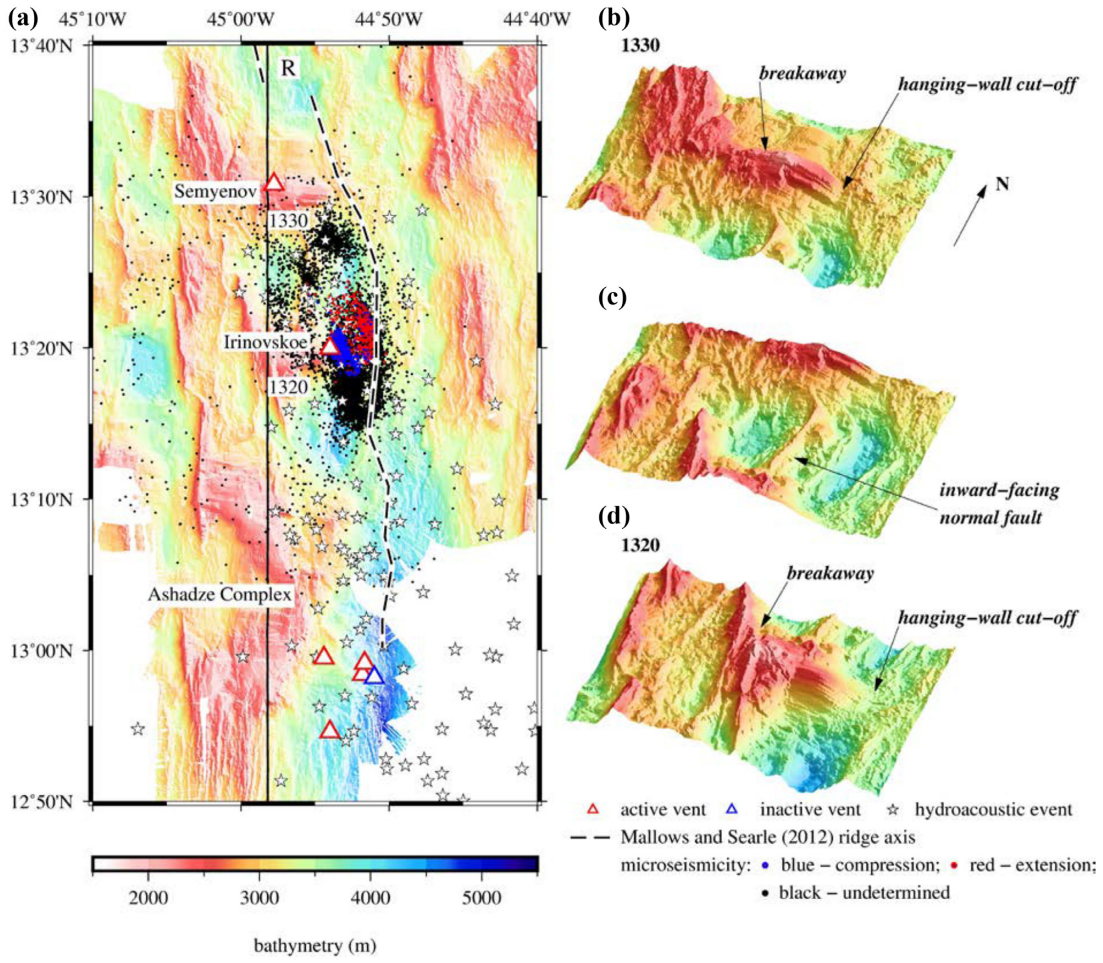

Figure 2. Features of the 13°N region of the Mid-Atlantic Ridge. (a) Illuminated high-resolution swath bathymetry (*cf.* Fig. 1c) showing the location of hydrothermal vents (labelled) relative to corresponding OCCs. Hydroacoustically detected seismicity is marked by open black stars (Smith *et al.* 2006), and a representative subset of the recorded microseismicity (after Parnell-Turner *et al.* 2017) is shown by black, red (extensional mechanisms) or blue (compressional) dots. Mallows & Searle's (2012) average ridge axis is marked by the white-black dashed line, and the solid black line locates Profile R. Perspective view of (b) the 1330 OCC showing the location of its breakaway and hanging-wall cut-off; (c) the inward-facing normal fault in the magmatic region between OCCs; and (d) the 1320 OCC showing the location of its breakaway. Note its well-defined corrugated detachment surface, and concave to the north and convex to the south hanging-wall cut-off.

(Cherkashov *et al.* 2010a), implying an off-axis underlying heat source.

The 13°N segment is bounded to the north by the Fifteen-Twenty FZ, and to the south by the Marathon TF-FZ system, with the Mercurius FZ located ∼50 km further south. At the southern ridge-transform intersection, between the 13°N segment and Marathon FZ, there is a prominent inside corner high (Peirce *et al.* 2019a and references therein). The 1330 OCC lies in the equivalent location of an inside corner with respect to a deviation in trend in ridge axis morphology to its north (Fig. 1).

The *P*-wave velocity–depth and density-depth crustal structures along an ∼200 km-long 2-D transect traversing all of these features—Profile R—was described by Peirce *et al.* (2019a). The primary conclusion of that study was that each OCC is structurally distinct and is exhumed along its own detachment fault. The crust was also inferred to be thinner between OCCs than beneath, with the two closely spaced OCCs of the Ashadze Complex exhibiting similar crustal structures at depth, such that they may now be linked, despite the north and south sections having quite distinct shallow crustal velocity and density profiles. The *P*-wave velocity–depth structure also indicated that the now relict Ashadze Complex and 1330 OCCs most likely have lower crust or serpentinized ultramafic lithologies exhumed to shallow, even seabed, depth, while the upper crust of the 1320 OCC comprises predominantly basaltic lithologies consistent with its still active stage of development. The *P*-wave study also showed that Marathon FZ appears to have a thin crust underlain by a 2–3 km-deep, ∼20 km-wide zone of serpentinized upper mantle. The primary goal of this study is to test these conclusions by determining the *S*-wave velocity structure, and then use the V_p/V_s ratio (citing the equivalent Poisson's ratio) to provide better constraint on both the lateral and vertical variation in structure with depth, inform lithology within the crustal section, and investigate the extent of fluid flow-induced alteration.

3 DATA ACQUISITION AND CHARACTERISTICS

JC132 (Reston & Peirce 2016) took place in January and February 2016. Details of the seismic, gravity and bathymetry data sets are

provided in Peirce *et al.* (2019a). For Profile R, contemporaneous acquisition of wide-angle (WA) ocean-bottom seismograph (OBS) and multichannel seismic (MCS) data was undertaken with a 60 s shot interval to prevent water wave wrap-around interfering with first arriving phases recorded by the OBSs, while still achieving an effective MCS reflection data fold of 20 by super-binning of adjacent traces within gathers. The seismic source consisted of a 12 Bolt airgun array of 4300 in^3 (70.5 L) volume, fired at 2000 psi (142 bar), and towed at 8 m depth.

WA seismic data along Profile R were recorded by 14 OBSs deployed between ~7 and 15 km apart along profile depending on the seabed topography (Fig. 1a). The largest inter-OBS gap coincides with the Marathon FZ, due to the water depth there exceeding the maximum instrument operational depth. In addition, data recorded by four further OBSs deployed along a co-incident profile within the 3-D grid survey (Fig. 1a; Simão *et al.* 2016 and the forthcoming Simão *et al.* 2020) were also included in the modelling of Profile R. WA data were recorded over 60 s trace lengths at 4 ms (250 Hz) sampling interval with a hydrophone and three-component geophone set. Variations in seabed topography and instrument-seabed coupling control the signal-to-noise ratio (SNR), as well as the primary traveltime characteristics of seismic phases recorded by each instrument.

Figs 3 and 4 show example record sections from OBSs 12, 65 and 69 (Fig. 1a). For OBS 12 (Figs 3a and b), for example, located on the southern flank of the 1320 OCC, secondary arriving phases identified as crustal *S*-wave refracted arrivals (Sg) converting at the seafloor, are only observed to offsets of <15 km to the south of the instrument location, despite *P*-wave refracted first arrivals (Pg) being recorded to offsets of ~30 km to both the north and south. This characteristic is common to each OBS record section along profile, from the north end of the profile to OBS 64 (Fig. 1a), located on the southern edge of the Ashadze Complex. Further south, Sg is more prominent (e.g. OBS 65; Figs 3c and d), being observed to both the north and south of each OBS out to shot-receiver offsets of ~40 km. There is little unequivocal evidence for mantle refracted arrivals (either Pn or Sn) or Moho reflections on any OBSs between OBS 12 and the north flank of Marathon FZ, sited on lithosphere less than ~1 Myr-old.

Each OBS located on 8-Myr-old lithosphere between FZs (e.g. OBS 69; Fig. 4) recorded *P*-wave arrivals out to offsets of ~55 km for shots fired from the south. For shots fired to the north of these instruments, arrivals were recorded only to offsets of ~30 km. However, corresponding *S*-wave (Sg) arrivals are only observed to ~40 km shot-receiver offset, and only for shots fired from the south. No primary *S*-waves were recorded by OBSs 13, 61 and 63 (Fig. 1a).

Fig. 4 shows a comparison between hydrophone and horizontal geophone (X) component record sections for OBS 69 (Fig. 1a). Here the *S*-waves appear to terminate at offsets coinciding with the FZ locations, which is also a feature common to record sections where either FZ lies within ~60 km shot-receiver distance from an OBS.

4 2-D MODELLING

4.1 WA seismic data modelling

S-wave (Sg) arrival traveltimes were picked, wherever possible, using unfiltered data, using a compare and contrast approach between horizontal geophone and hydrophone record sections for each instrument. Fig. 5 shows a representative example with both *P*- and *S*-wave arrivals recorded. Given the largely sediment-free seabed, significant seabed scattered signal is observed in the record sections behind the primary *P*-wave first arrival. When coupled with a quite reverberative source signature, this made traveltime picking of the secondary arriving *S*-wave, to a degree of accuracy suitable for inversion purposes, difficult using the horizontal channels alone. Consequently, as the hydrophone channel displayed the highest SNR, the hydrophone record section was used as an arrival marker against which picks were made and/or checked against a horizontal component. Since the hydrophone was mounted on each OBS <0.3 m above the seabed (i.e. <0.3 m of the total *S*-wave arrival path would be as a *P*-wave) this indicative framework picking approach was deemed acceptable within the overall location and pick errors. A pick uncertainty of 100 ms was assigned to each of the ~2400 *S*-wave arrival traveltime picks, regardless of shot-receiver offset and, thus, turning depth within the crust or mantle. This pick uncertainty largely represents the shot and receiver location error and the ability to determine *S*-wave onset time in the presence of the *P*-wave wave train and background noise.

The *FAST* method of Zelt & Barton (1998) was adopted for traveltime inversion, using the approach outlined in Peirce *et al.* (2019a) for the *P*-wave model derived for Profile R. The model was discretized on a 0.25 km by 0.25 km uniform square mesh (forward cell size). The seabed interface, kept fixed throughout inversion, was created by sampling the bathymetry data at 0.25 km intervals along profile, and projecting this and the OBS and shot locations into kilometre distance along profile relative to a model 0,0 located at 11°56.76′N/44°58.2′W (Fig. 1a). As no sediment cover of any significant thickness was observed along profile (see seismic reflection section in Peirce *et al.* 2019a), any initial inversion model would comprise a simple 1-D velocity–depth profile applied beneath the seabed. Other than the seabed itself, no first-order velocity discontinuity was imposed anywhere within the model.

Zelt & Barton (1998) state that, for *FAST*, the 'selection of starting model is important because the assumption of the linearization is that small perturbations to the starting model are determined'. As such, first, an *S*-wave-type velocity initial model (Fig. 6a) was constructed by dividing Peirce *et al.*'s (2019a) *P*-wave model (Fig. 6c) by 1.7. This model, regardless of inversion parameter choice, failed to iterate effectively away from the initial start point, sufficient to be sure that it did not represent a preconceived bias as to inversion outcome. Consequently, an additional range of initial models was also tested, with the velocity immediately below the seafloor varying between 2.0 km s^{-1} and 4.0 km s^{-1}, and increasing to 7.5 km s^{-1} at ~5 km subseabed. Below this depth, the velocity was increased to 8.5 km s^{-1} at ~10 km subsea level to represent a constant-depth Moho. Regardless of the chosen velocity immediately subseabed, all of these initial models resulted in equivalent outcomes in terms of velocity–depth structure. Consequently, the highest velocity end-member starting model (the *P*-wave initial model of Peirce *et al.* 2019a—henceforth the *initial model*; Fig. 6c) was chosen such that it represented no preconceived idea of crustal *S*-wave structure from the outset.

The inversion process comprised one run of five nonlinear iterations with a 1.5 × 1.5 km inverse cell size, followed by one run of three iterations, with a 0.75 × 0.75 km cell size. A summary of the inversion parameters is provided in Table 1, together with those for the corresponding *P*-wave model (Peirce *et al.* 2019a) for comparison. The differences in inversion cell sizes are a direct consequence of the sparser ray coverage, due to the fewer *S*-wave traveltime picks, and have little effect on the inversion outcome. For the first run, a χ^2 of ~14.8 and root mean square traveltime misfit

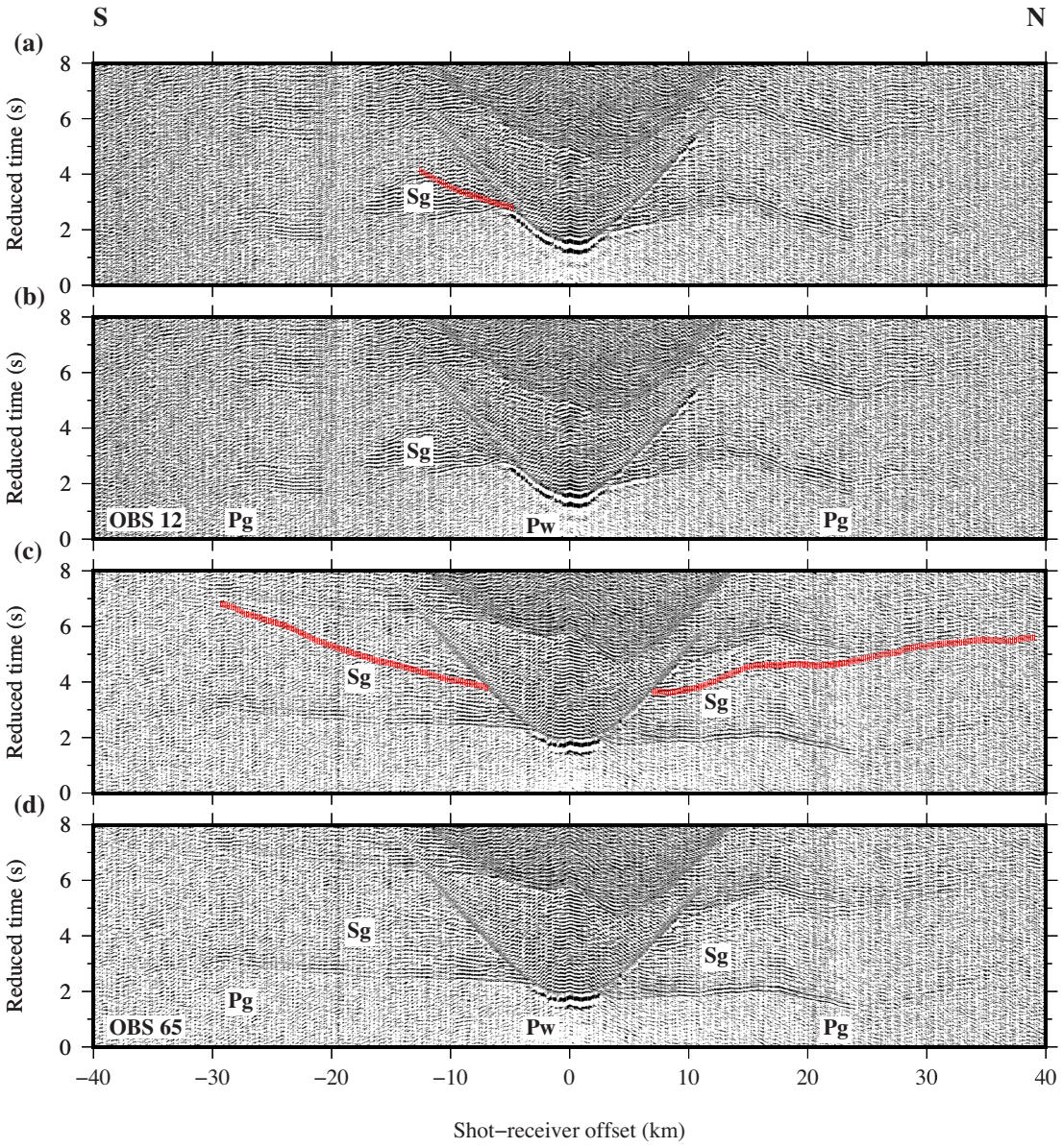

Figure 3. Example hydrophone record sections for OBSs 12 (a and b) and 65 (c and d). See Fig. 1(a) for location. Record sections show filtered hydrophone data plotted at a reduction velocity of 6 km s^{-1}. *S*-wave traveltime picks have been plotted as red bars equivalent to the pick uncertainty (100 ms) in length. Crust (Pg and Sg) and water wave (Pw) phase identifications are annotated.

of 384 ms were achieved (Fig. 7b), where a χ^2 of 1 signifies a fit to the traveltime pick error. This model was used as the starting point for the second run, which resulted in a traveltime misfit of 279 ms, equivalent to a χ^2 of ∼7.8 (Fig. 7c) which, primarily, suggests that the traveltime pick errors have been underestimated to a minor extent.

The final inversion model (Fig. 7c) shows that each OCC has a distinct velocity structure, with higher velocity at shallow crustal level beneath the northern Ashadze Complex in particular. Both the 1320 and 1330 OCCs have a low *S*-wave velocity throughout the upper crust. The most notable feature of this model, though, lies throughout the region to the south of the Ashadze Complex and, in particular, beneath Marathon FZ. Here, an *S*-wave velocity of ∼2 km s^{-1} is observed to significant subseabed depth. The features of this model, henceforth called the *S-wave inversion model*, will be considered further in Section 5.

4.2 Inversion model resolution testing

To determine the smallest structures and velocity variations resolvable in the *S-wave inversion model* we performed checkerboard testing (Fig. 8), following the approach of Zelt (1998). In this process, a velocity perturbation was added to the *S-wave inversion model* and synthetic traveltimes calculated using the shot-receiver offsets of the observed traveltime picks. Random Gaussian noise corresponding to the pick uncertainties was then added to the synthetic traveltimes, prior to their inversion using the same parameters as those used to derive the *S-wave inversion model* itself (Table 1).

Input checkerboards were applied with a range of different vertical and horizontal cell sizes and scales of velocity perturbation, expressed as a percentage of the background model velocity. In order to remove any potential effects of input checkerboard pattern geometry on the outcome of testing, a suite of 14 unique patterns was

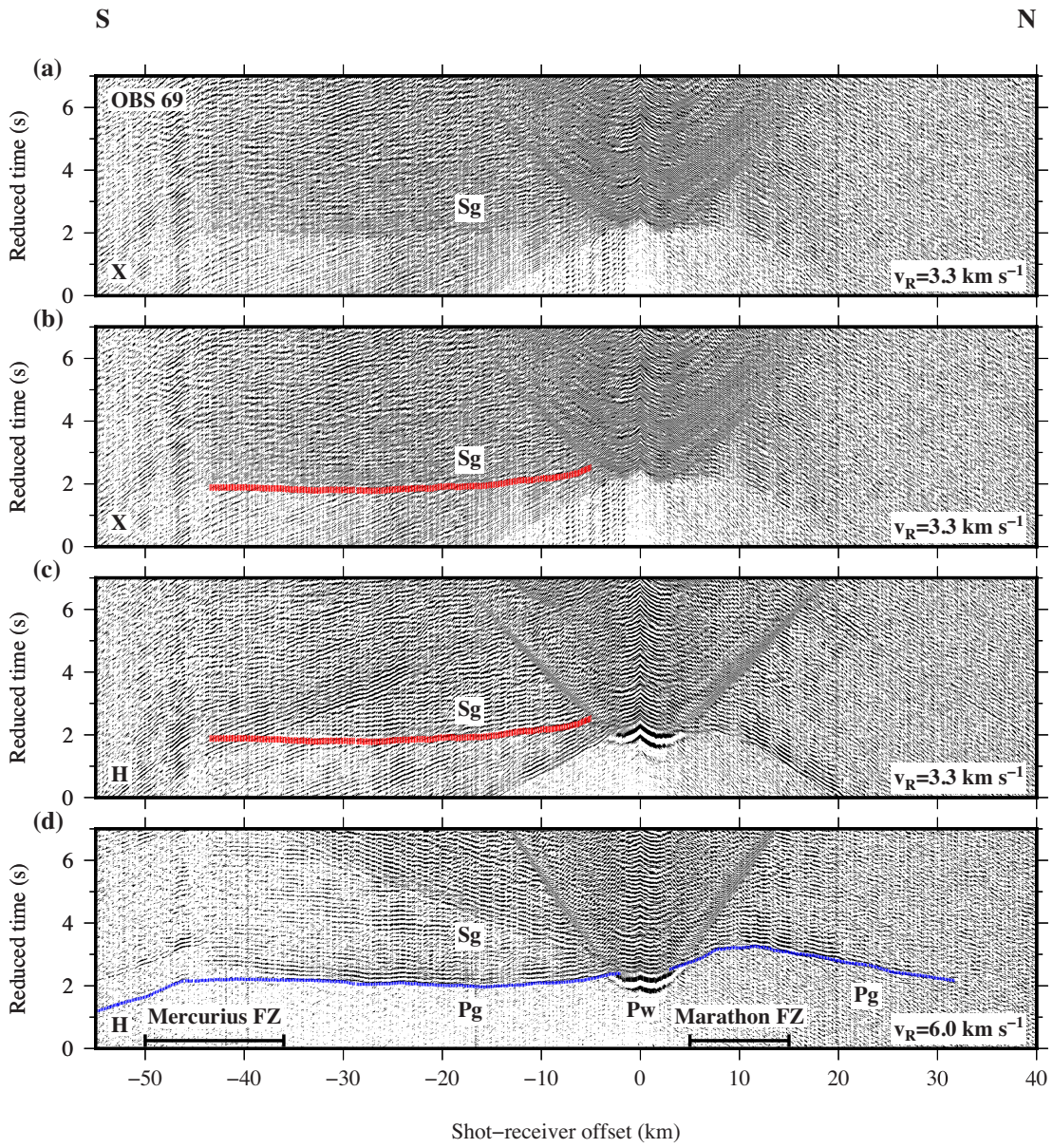

Figure 4. Example horizontal geophone (a and b; X component) and hydrophone (c and d) record sections for OBS 69. See Fig. 1(a) for location. Record sections show filtered data plotted at the annotated reduction velocity (V_R). *S*-wave traveltime picks have been plotted as red bars equivalent to the pick uncertainty (100 ms) in length, and *P*-wave traveltime picks as blue bars (50 ms). Crust (Pg and Sg) and water wave (Pw) phase identifications are annotated. The locations of Marathon and Mercurius FZs in relation to OBS 69 are also indicated, corresponding to a significant decrease in signal amplitude.

tested for each checkerboard size by applying half-checkerboard size phase shifts laterally and vertically, and reversing the velocity anomaly polarity (positive and negative). Here we show the 'at best' resolutions achieved for the upper mid-crust (Figs 8a–c) and the entire crust along profile (Figs 8d–f), and for the region beneath and between Marathon and Mercurius FZs (Figs 8g–i). In each case, the pattern recovery is demonstrated by the semblance (Zelt 1998) and is masked by the ray coverage, as indicated by the cell hit count (Fig. 7d). We adopt Zelt's (1998) semblance threshold of 0.7 to define areas of the model that are well resolved, even though semblance can be misleading as it is dependent on the operator radius. We use an operator radius set to the checkerboard cell size, which is larger than the inverse cell size. Figs 8a–c show that, for an applied ±5 per cent velocity anomaly, structures larger than 5 km × 2 km should generally be resolvable to a depth of ∼2–3 km subseabed between 40–180 km along profile, where the semblance threshold of 0.7 is exceeded (Fig. 8c), particularly beneath the 1320 and 1330 OCCs, the northern OCC of the Ashadze Complex, and the outside corner.

In general, for the crust as a whole, a 7 km × 4 km checkerboard cell size consistently yields reasonable-to-good recovery along the entire profile (Figs 8d–f). However, caution needs to be taken when considering this cell size pattern as, in places, the vertical dimension matches the crustal thickness or the entire depth range of ray coverage. However, laterally the pattern is smaller than OCC width and inter-OCC spacing at the seabed and can thus be used to inform resolution of axis parallel inter-OCC connectivity. For all checkerboard patterns less than 10 km-wide horizontally, little pattern recovery was achieved in the vicinity of Marathon FZ. Consequently, the 'at best' smallest scale of feature recoverable here

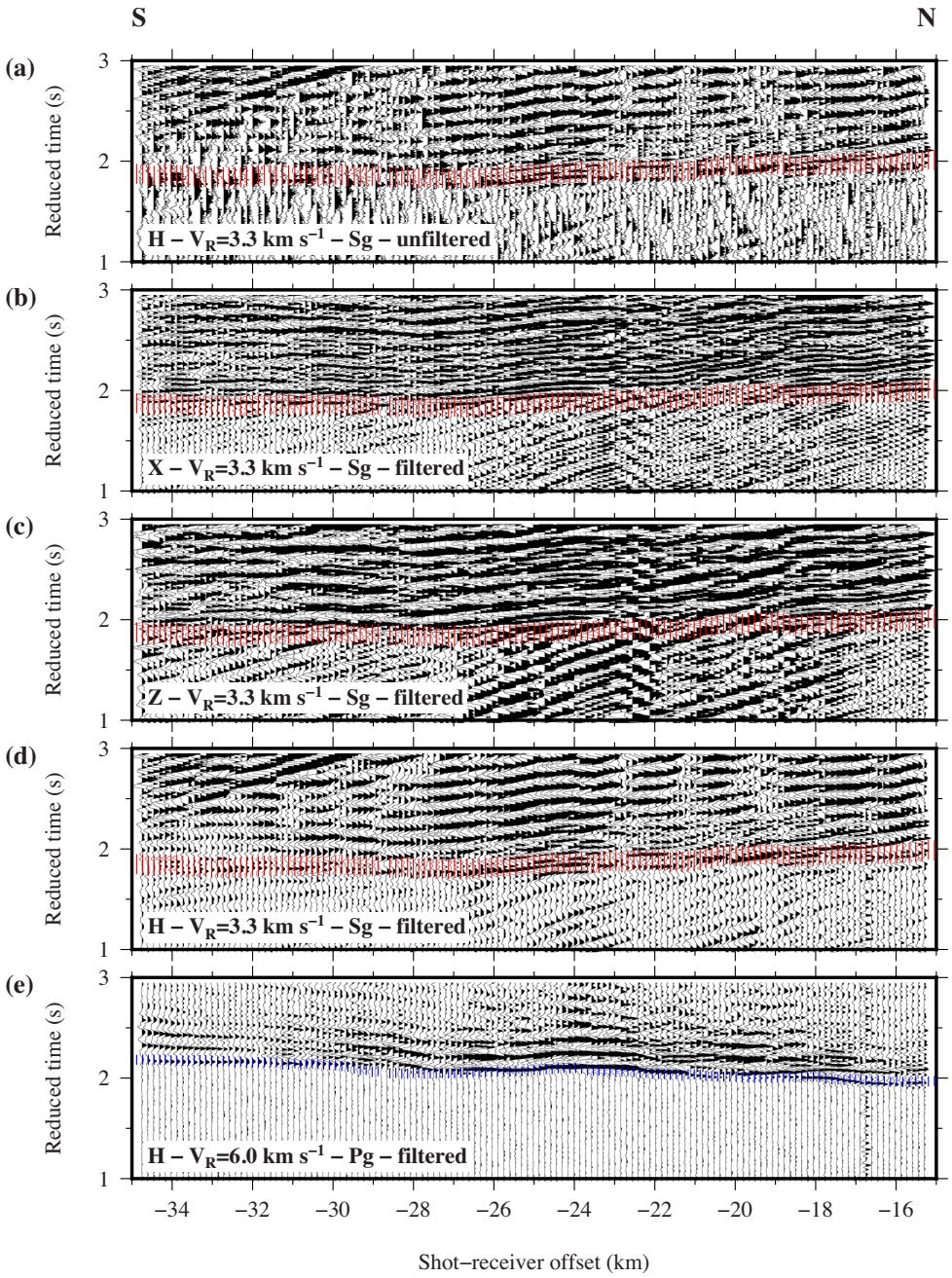

Figure 5. Example record sections for OBS 69. See Fig. 1(a) for location. (a–c) Geophone and (d) hydrophone record sections (channel as annotated) plotted to show *S*-wave arrival traveltime picks (red). (e) Hydrophone data plotted to show the corresponding *P*-wave traveltime picks (blue). Reduction velocities (V_R) are indicated. Traveltime picks have been plotted as bars equivalent to the pick uncertainty (*P*-wave 50 ms; *S*-wave 100 ms) in length. Crustal (Pg and Sg) phase identifications are annotated. Traveltime picking was undertaken predominantly using unfiltered data.

is larger than 10 km × 2 km and ±5 per cent velocity anomaly (Figs 8g–i).

Ray coverage and/or the recovery of the imposed checkerboard are consistently poorest below 7 km below sea level and to the north of 120 km along profile distance, reflecting the apparent absence of longer-offset observed arrivals. Consequently, this marks the depth to which the model may be interpreted with any confidence. Overall, though, the resolution testing indicates that the internal velocity structure of each OCC should be independently resolvable and, consequently, so should their along ridge axis inter-relationship. Testing also showed that the general velocity characteristics of Marathon FZ and the northern flank of Mercurius FZ are resolved at a scale of 10 km × 2 km despite the relatively limited *S*-wave propagation across them, particularly at depth.

4.3 Model features

On the basis of the resolution testing and the *P-wave inversion* and *forward models* and *density models* of Peirce *et al.* (2019a), shown together for comparison in Fig. 9, the features of the *S-wave inversion model* were appraised to identify which were a consequence of

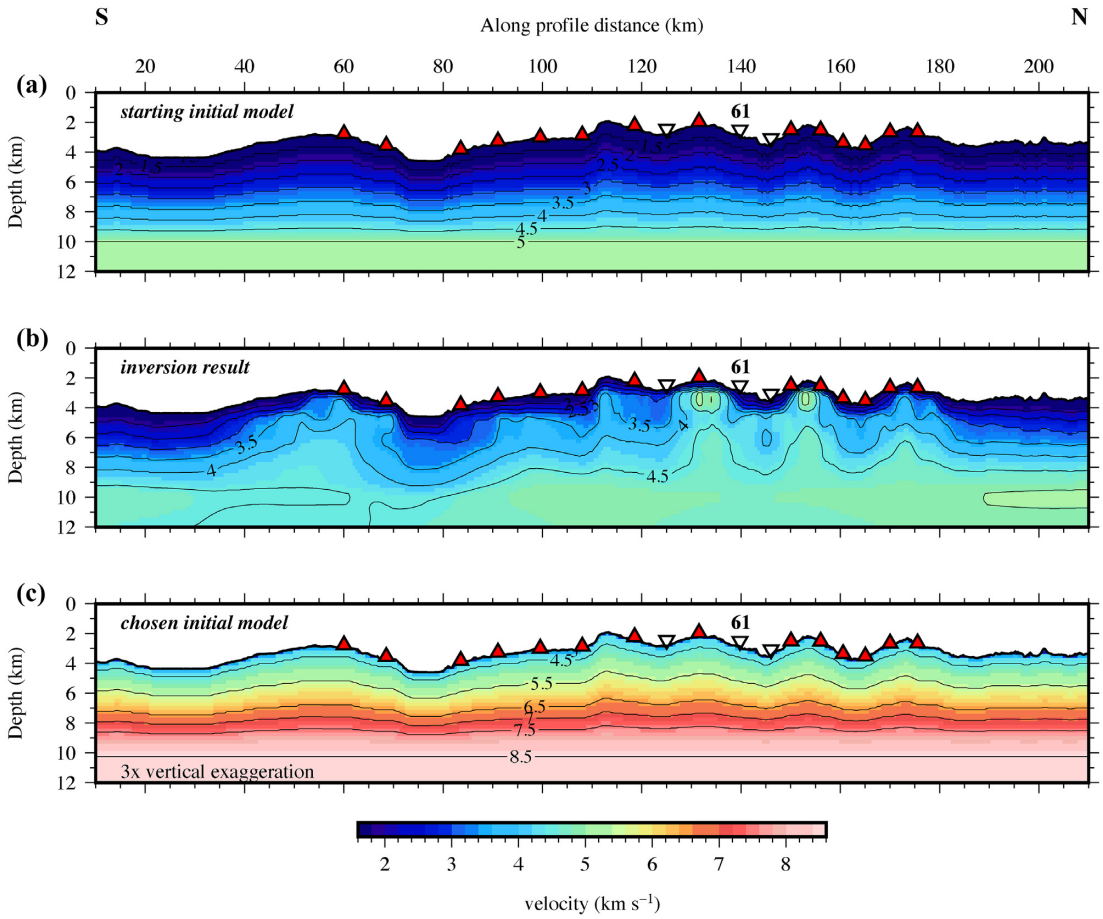

Figure 6. Inversion initial models. (a) *S*-wave-type initial model constructed using a 1-D velocity–depth profile beneath the seabed. (b) Result of inversion using the initial model in (a) as the starting point. Regardless of parameter choice the inversion fails to effectively iterate away from the starting point shown in (a). (c) Peirce *et al.*'s (2019a) *P*-wave *initial model* chosen as the starting point for the *S*-wave inversion. See text for discussion. In all parts, OBS locations are marked by red triangles, with inverted unfilled triangles locating OBSs that did not record *S*-waves.

Table 1. Summary of *P*-wave and *S*-wave inversion parameters (after Zelt & Barton 1998).

Inversion parameter		*P*-wave model (after Peirce *et al.* 2019a)	*S*-wave model
sz		0.125	0.125
α		0.95	0.95
λ_0		100	100
λ reduction factor		1.414	1.414
Forward cell size		0.25 × 0.25 km	0.25 × 0.25 km
Inversion cell—first phase	horizontal	1.0 km	1.5 km
	vertical	1.0 km	1.5 km
Inversion cell—second phase	horizontal	0.5 km	0.75 km
	vertical	0.5 km	0.75 km

real geological structure and which result from the inversion process. An alternative way to appraise the lateral and vertical variation in velocity within models is to calculate the difference-from-average *P*-wave and *S*-wave models as shown in Fig. 10. The difference in velocity between each cell in each horizontal layer below sea surface (specified as the forward cell size vertical dimension of 0.25 km) and the average for that layer (i.e. collectively forming a 1-D average velocity–depth profile) was calculated (following Dunn *et al.* 2017) using only those cells within each layer that are constrained by ray paths traced from shot to receiver. This approach, for example, highlights the location, and vertical and lateral extents within the crust of the Marathon FZ, and regions where lower crustal and uppermost mantle lithologies have been exhumed to shallower crustal levels to varying extents along axis beneath OCCs, by a positive difference in the V_p/V_s ratio (and similarly in the Poisson's ratio).

Few model artefacts remain in the *S-wave inversion model* after the second stage of inversion. A small localized bull's eye

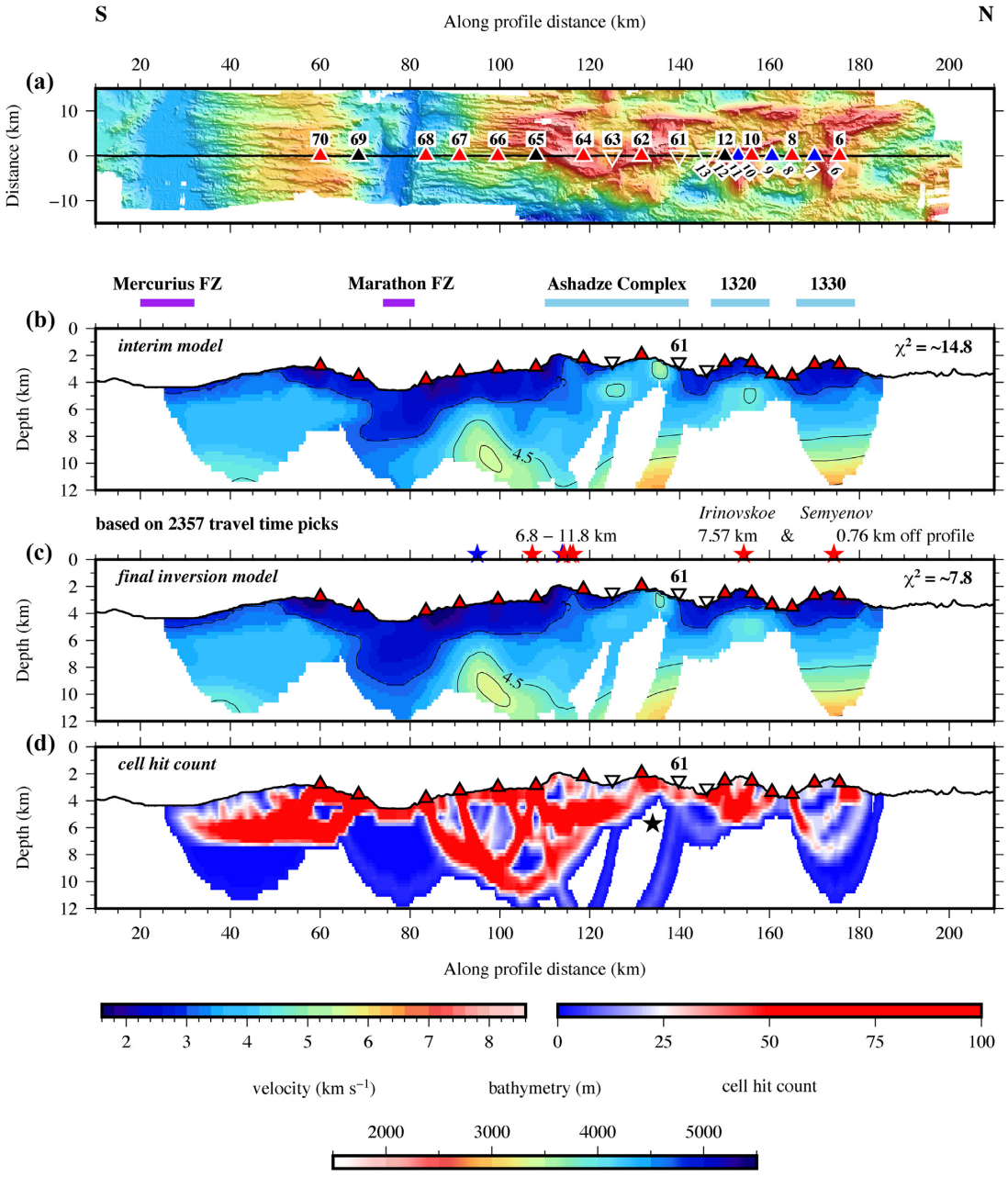

Figure 7. Inversion modelling. (a) Acquisition geometry showing the bathymetry, shots fired (solid black line) and OBSs (triangles). Inverted unfilled triangles locate OBSs which did not record *S*-waves. OBSs annotated in italics recorded a co-incident profile from the 3-D grid and have been included in the analysis. The record sections for OBSs highlighted in black are shown in Figs 3–5. (b) Interim model achieved after the first inversion run within an inverse cell size of 1.5 km × 1.5 km. (c) Final *S-wave inversion model* achieved after a further run with a cell size of 0.75 km × 0.75 km. See Table 1 for inversion parameters. Hydrothermal vents (red star = active; blue star = inactive) are annotated above with their off-profile distance. (d) Cell hit count indicatively showing the areas of the model covered with rays traced as part of the inversion process. The black star marks a prominent gap in ray coverage that extends to shallow subseabed depth. Panels (b) and (c) are masked to show only areas with ray coverage.

feature at the offset, depth 132,4 km (Figs 9c and 10b), is associated with the location of OBS 61, for which no *S*-wave arrivals were observed, while a region of higher velocity centred at 95,9 km (Fig. 9c), matching no feature in either of the *P-wave forward* or *inversion models* (Figs 9a and b, respectively), is considered to be a trade-off compensation feature resulting from a gap in the ray coverage (Fig. 7d). We propose that the remaining features, in parts of the model with semblance ≥0.7, all represent robust features of the traveltime data. The principal crustal characteristics, which will be discussed in geological context in Section 6, are as follows:

(i) the northern Ashadze Complex is underlain by a higher *S*-wave velocity (>3.5 km s^{-1}) at shallower crustal depth than any of the other OCCs of the western flank,

(ii) the 1320 and 1330 OCCs are distinguished by a region of higher *S*-wave velocity (>3.0 km s^{-1}) at shallower crustal depth beneath the former,

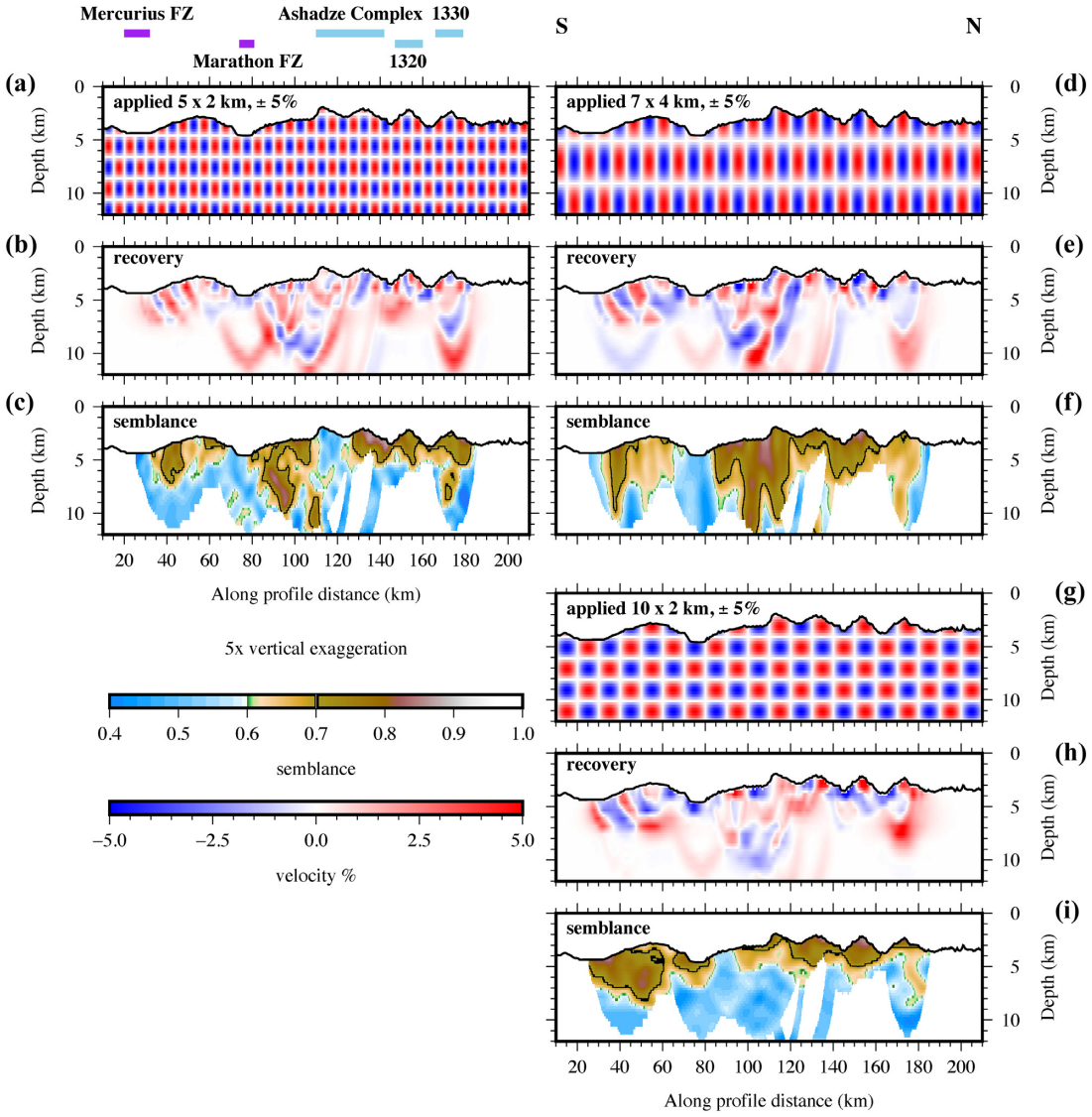

Figure 8. Resolution testing of the *S-wave inversion model* (*cf.* Fig. 7c). (a) Applied 5 km × 2 km ± 5 per cent velocity anomaly checkerboard. Prominent topographic features are annotated above. (b) Checkerboard recovery. (c) Corresponding semblance, showing that the inversion process resolves features of this scale and velocity throughout the upper crust along the majority of the profile. (d) Applied 7 km × 4 km ± 5 per cent velocity anomaly checkerboard. (e) Checkerboard recovery. (f) Corresponding semblance, showing that the inversion process resolves features of this scale throughout the crust apart from beneath Marathon and Mercurius FZs. (g) Applied 10 km × 2 km ± 5 per cent velocity anomaly checkerboard. (h) Checkerboard recovery. (i) Corresponding semblance, showing that the inversion process resolves features of this scale beneath Mercurius FZ. The thin black contour in all semblance panels indicates which parts of the model are well recovered using a semblance of 0.7 as the threshold criterion. All checkerboard recovery and semblance plots are masked to show only areas with ray coverage (*cf.* Fig. 7d).

(iii) the 1330 OCC has a lower *S*-wave velocity than any other OCC,

(iv) the outside corner to the north of Marathon FZ has a low *S*-wave velocity (<3.0 km s^{-1}) to mid-crustal depth,

(v) Marathon FZ is underlain by a region of ∼2 km s^{-1} *S*-wave velocity throughout the upper crust, and

(vi) the inside corner to the south of the Marathon FZ has an *S*-wave velocity–depth structure similar to that of the 1330 OCC, but distinctly different to that of the 1320 OCC.

5 V_p/V_s AND POISSON'S RATIOS

The V_p/V_s and Poisson's (σ) ratios are often used as seismic-derived proxies for lithology and degree of metamorphism. For example, Christensen (1996) cites $\sigma \approx 0.28$–0.30 as indicative of normal ridge axis oceanic crust and further propose that $\sigma >$ 0.34 indicates serpentinized lithologies. Grevemeyer *et al.* (2018a) apply the proxies $V_p/V_s < 1.9$ for magma-rich and >1.9 for magma-poor crustal formation, while Grevemeyer *et al.* (2018b) use $V_p/V_s > 1.8$ to delineate areas of increased serpentinization and hydration.

Plotting V_p versus V_s for basalts/gabbros and for serpentinites (e.g. Carlson & Miller 1997; Christensen 2004) reveals that the two trends cross at $V_p \approx 7.5$ km s^{-1}. Considering the precision in the velocity estimates, discrimination on the basis of V_p/V_s alone is valid for a V_p below ∼7 km s^{-1}, where $V_p/V_s > 1.85$ indicates serpentinites and <1.85 magmatic crust. In the same range, Poisson's ratio for serpentinites is >0.3, whereas for magmatic crust

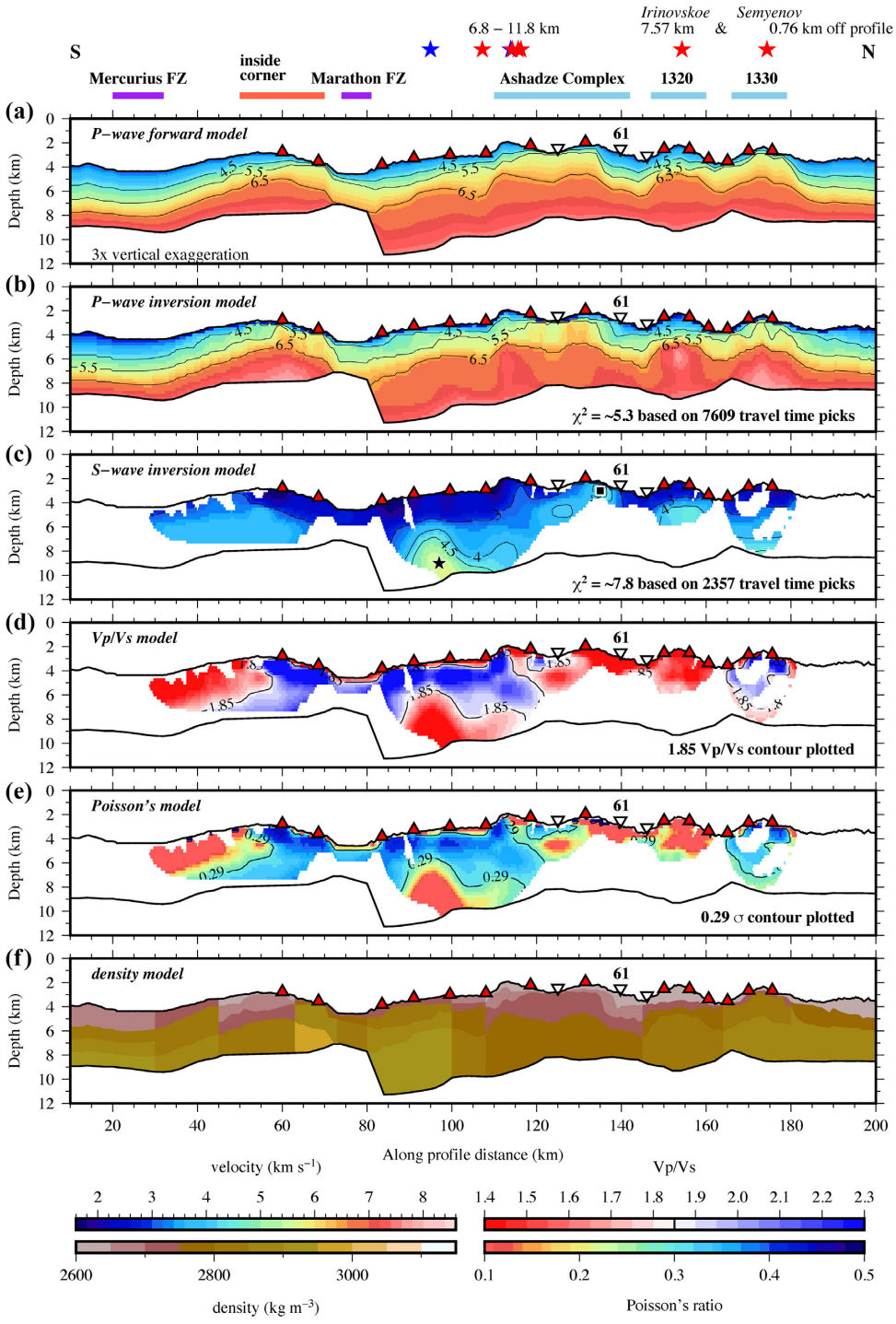

Figure 9. Model comparison. (a) *P-wave forward model* derived from (b) the *P-wave inversion model* using the 5.5, 6.5 and 7.5 km s^{-1} contours used by Peirce *et al.* (2019a) to define interface boundaries. OBS locations are marked by red triangles, with inverted unfilled triangles locating OBSs (e.g. OBS 61) which did not record *S*-waves. Prominent topographic features and hydrothermal vents (red star = active; blue star = inactive) are annotated above. (c) *S-wave inversion model* with areas marked by a black star and black square interpreted as artefacts of the inversion process (see the text). Velocity contours are annotated. The *P-wave* and *S-wave inversion models* were used to calculate the V_p/V_s and Poisson's ratios. (d) V_p/V_s *model* with the 1.85 contour marked that acts as a proxy for lithology type and degree of hydration (Grevemeyer *et al.* 2018a,b; Peirce *et al.* 2019b). (e) *Poisson's model* with the equivalent 0.29 proxy contour marked. (f) *Density model* (after Peirce *et al.* 2019a). Panels (c)–(e) are masked to show only areas with ray coverage (*cf.* Fig. 7d) and a *P*-wave velocity of <7.0 km s^{-1}, and all parts are also masked by the base of crust determined from gravity modelling (f).

it is <0.28. Consequently, either of these proxies should highlight any along ridge variation in OCC lithological characteristics, degree of hydrothermal alteration, extent of lower crust and uppermost mantle exhumation, and potential tectonic and magmatic conditions that trigger the development of an OCC and which, ultimately, dictate its decline. In addition, the same proxies can also be applied to fracture zones to constrain the extent (both lateral and vertical) of fracturing and faulting, and the

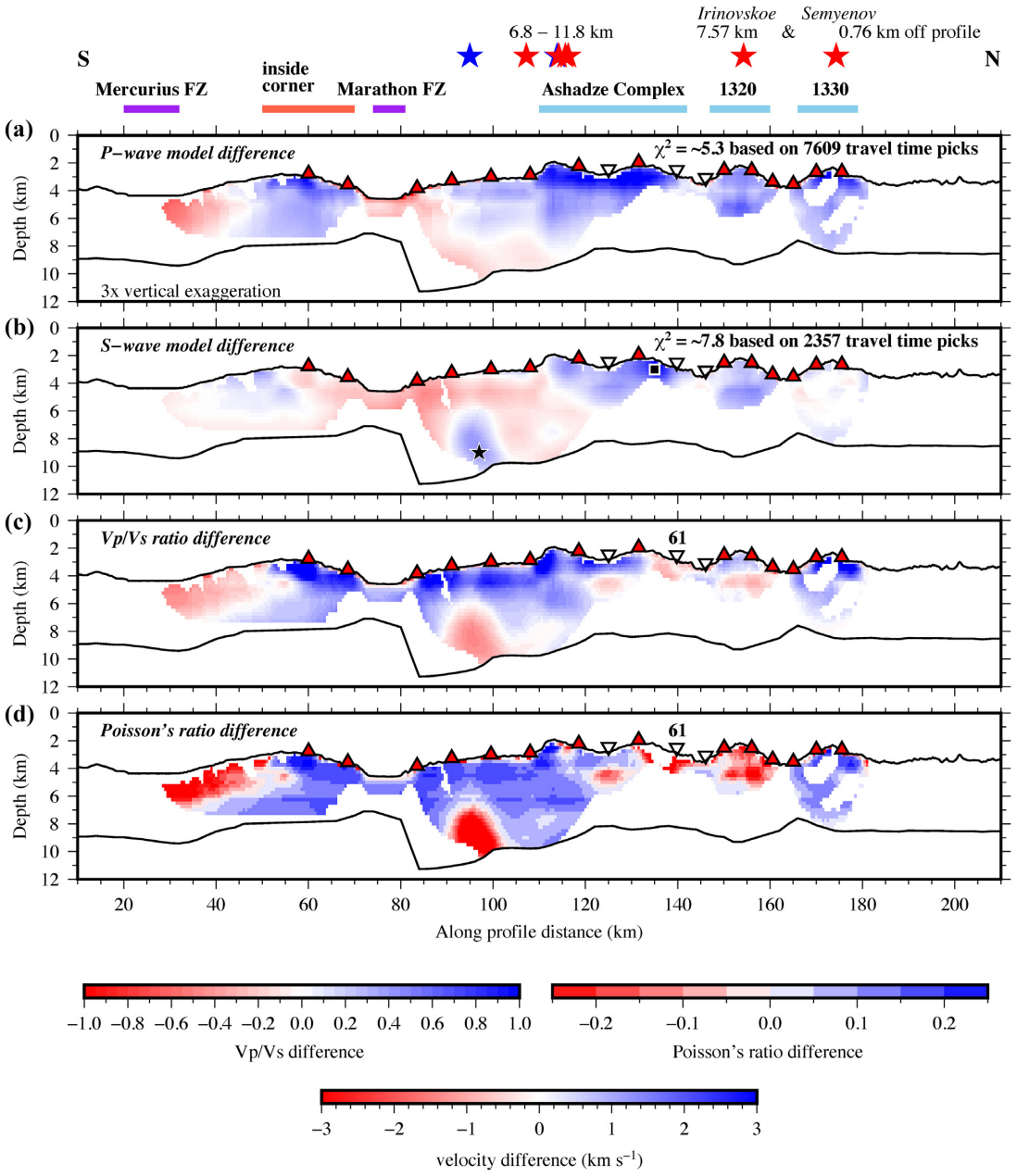

Figure 10. Differences-from-average model representations. OBS locations are marked by red triangles, with inverted unfilled triangles locating OBSs (e.g. OBS 61) which did not record *S*-waves. Prominent topographic features and hydrothermal vents (red star = active; blue star = inactive) are annotated above. (a) *P-wave inversion model*. (b) *S-wave inversion model*. (c) V_p/V_s *model*. (d) *Poisson's model*. Each of these models show the difference-from-average within vertical cell-sized horizontal slices, demonstrating the variation in crustal structure ridge parallel, and particularly highlighting regions interpreted to reflect lower crustal and uppermost mantle lithologies exhumed to the vicinity of the seabed. All parts are masked to show only areas with ray coverage (*cf.* Fig. 7d) and a *P*-wave velocity of <7.0 km s^{-1}, and the base of crust determined from gravity modelling (*cf.* Fig. 9f). The black star and black square mark features interpreted as artefacts of the inversion process (see Fig. 9 and the text).

degree of fluid ingress occurring through such a fracture network to metamorphose the lower crust and serpentinize the uppermost mantle.

To enable direct comparison with previous studies, both the V_p/V_s and Poisson's ratios were, therefore, calculated along Profile R using the *P-wave* and *S-wave inversion models*, for areas where both models are constrained by *P*- and *S*-wave ray paths. These models (henceforth the V_p/V_s *model* and *Poisson's model* respectively) are shown in Fig. 9 and their corresponding difference-from-average displays in Fig. 10. We highlight the Poisson's ratio and V_p/V_s contours of 0.29 and 1.85 respectively, and mask areas of the model where $V_p > 7$ km s^{-1} or ray coverage is low (<25 per cell). The lithological prediction derived from the V_p/V_s ratio (or equivalent Poisson's ratio) allows us to interpret the crustal section with

some confidence. A number of primary correlations with tectonic structure are evident, all compatible with V_p and density (Peirce *et al.* 2019a), and each will be discussed in geological context in Section 6. From north to south:

(i) the 1330 OCC V_p/V_s ratio of >1.9 (Poisson's ratio of >0.34) can be interpreted to suggest that the bulk of the crust beneath this OCC comprises serpentinized lithologies that have been exhumed to the shallowest crustal level,

(ii) the 1320 OCC the V_p/V_s ratio of <1.8 (Poisson's ratio of <0.2) suggests that this OCC is underlain by mafic lithologies to mid-crustal depth, but the profile only crosses the blocky portion of the OCC just ridgeward of the breakaway and does not cross the corrugated portion of the OCC where mantle serpentinites might be expected,

(iii) the V_p/V_s ratio in the transition between the 1320 and 1330 OCCs suggest that the shallow crust is dominated by magmatic rocks, that continue southwards towards the Ashadze Complex, in a layer no thicker than the upper crustal vertical resolution of 2 km,

(iv) the north and south OCCs of the Ashadze Complex have contrasting structures at shallow crustal depth, with the north OCC having a significantly faster (by ∼2 km s^{-1}) *S*-wave velocity in the upper crust (and hence lower V_p/V_s ratio consistent with mafic crust). Between the north and south parts of the Complex, the profile crosses a slight bathymetric depression marked by corrugated seafloor, just westward of the most recent breakaway. For 1 km immediately beneath the corrugated seafloor the V_p/V_s ratio is high, indicative of serpentinized peridotite, but itself is underlain by a 2-km-thick zone of low V_p/V_s ratio, most likely reflecting a mafic intrusion. As the profile continues over the southern edge of the Complex, it passes over a convex-outward scarp, the likely breakaway of the most recent detachment. The blocky crust here has a predominantly low V_p/V_s ratio (considering the shallow crustal lateral and vertical resolution of 2 km) and is, therefore, most likely magmatic,

(v) south of Ashadze Complex, a thin layer (no thicker than the upper crustal vertical resolution of 2 km) with a low V_p/V_s ratio is underlain by a pronounced and laterally continuous, 2–4-km-thick layer with a high V_p/V_s ratio. Although at the resolution limits, we interpret this region as a thin layer of volcanics either rafted with or emplaced through a large extent of unroofed, serpentinized mantle. Alternatively, this region may reflect the extent of deformation associated with the Marathon FZ that facilitates fluid ingress into the crust and supports metamorphism, and

(vi) the volcanic layer continues across the Marathon FZ, although its thickness there is not well constrained, and for ∼10 km to the south. The inside and outside corners to Marathon FZ display a high V_p/V_s ratio and lower density characteristics consistent with serpentinized mantle, similar to the 1330 OCC, beneath a thin layer of volcanics.

6 DISCUSSION

6.1 Transform faults and fracture zones

The outside corner to the north of the Marathon FZ shows low *S*-wave velocity at shallower depth in a pattern not dissimilar to that observed beneath the south Ashadze and 1320 OCCs, suggesting a generally amagmatic section of ridge axis, but one which demonstrates significant inward-facing normal fault-like morphology (Fig. 1). 1-D *P*-wave velocity–depth profiles (Peirce *et al.* 2019a) show that Marathon FZ has a relatively thin layer (∼1–2 km) with lower *P*-wave velocity throughout its bathymetric footprint. Beneath this lies an ∼2-km-thick region of, most likely, serpentinized uppermost mantle (Figs 9b and f). This study shows that the *S*-wave velocity is, correspondingly, very low. However, the width of the low-V_s zone extends beyond the footprint of the FZ itself, reaching up to ∼20 km laterally beneath the inside corner to the south, and for ∼40 km beneath the outside corner to the north up to the southern flank of the Ashadze Complex (Fig. 1a). This observation suggests significant metamorphism beneath the FZ bathymetric footprint, and that faulting and/or fluid circulation may also be laterally quite extensive.

Mallows & Searle (2012) interpret seabed morphology and fabric determined using TOBI sidescan sonar data and swath bathymetry (see fig. 2 of Peirce *et al.* 2019a) in the axial region between ∼13°15′N and 13°45′N (Figs 1a and c) as displaying an asymmetric spreading pattern, with greater fault slip to the west of the ridge axis south of ∼13°30′N, and to the east in the north. Gerya (2010, 2013) proposes that one consequence of asymmetric crustal formation is the spontaneous initiation of a transform fault along a pre-existing weakness. MacLeod *et al.* (2009) interpret the volcanic terrane to the north of ∼13°30′N as reflecting magmatic seafloor spreading, and Peirce *et al.*'s (2019a) *P*-wave velocity model supports that view showing a crust with a velocity–depth profile consistent with standard oceanic crustal envelopes (e.g. White *et al.* 1992), and having a distinct Moho.

The free-air, residual mantle Bouguer and magnetic anomalies (Peirce *et al.* 2019a) also suggest a different mode of crustal formation is occurring to the north of ∼13°40′N, bounded to the south by a westward step in neovolcanic zone at ∼13°38′N (Fig. 1c), interpreted by Mallows & Searle (2012) as a non-transform offset. The magmatism in the vicinity of the 1330 OCC, the apparent incipient dissection of the OCC behind (west of) the hanging-wall cut-off (Fig. 2b), and the concentration of a band of microseismicity (Parnell-Turner *et al.* 2017) on its southern flank (Fig. 2a), may be associated with ridge tip southward propagation and readjustment of ridge geometry along axis, with a corresponding evolution of a deviation in ridge linear trend into a small-offset transform discontinuity. In this context, the OCCs expressing more magmatic crustal structures lie within a newly distinct ridge segment forming to the south of the 13°45′N. Consequently, the 1330 OCC will eventually sit in an inside corner setting with respect to the ridge axis to the north, where the southern side of its detachment acts as the line of inherited fabric along which a transform is now evolving, and which results in a westward-stepping of the ridge axis.

6.2 Oceanic core complexes

The seismic and gravity models presented here reveal distinct crustal structures beneath each of the OCCs currently in the vicinity of the western flank of the ridge axis, generally showing varying degrees of elevated velocity at shallow subseabed depth, and contrasting density structures. Both the *P*-wave and *S*-wave velocity–depth models (Fig. 9) show that the upper crust of the 1320 OCC comprises predominantly basaltic lithologies, despite the reported exposures of gabbros and serpentinites (Escartin *et al.* 2017), while beneath the 1330 and southern Ashadze Complex OCCs, rocks of the lower crust or serpentinized ultramafic lithologies have been exhumed to, or within close proximity of, the seafloor. Although the northern Ashadze Complex OCC has a basaltic upper crustal velocity–depth

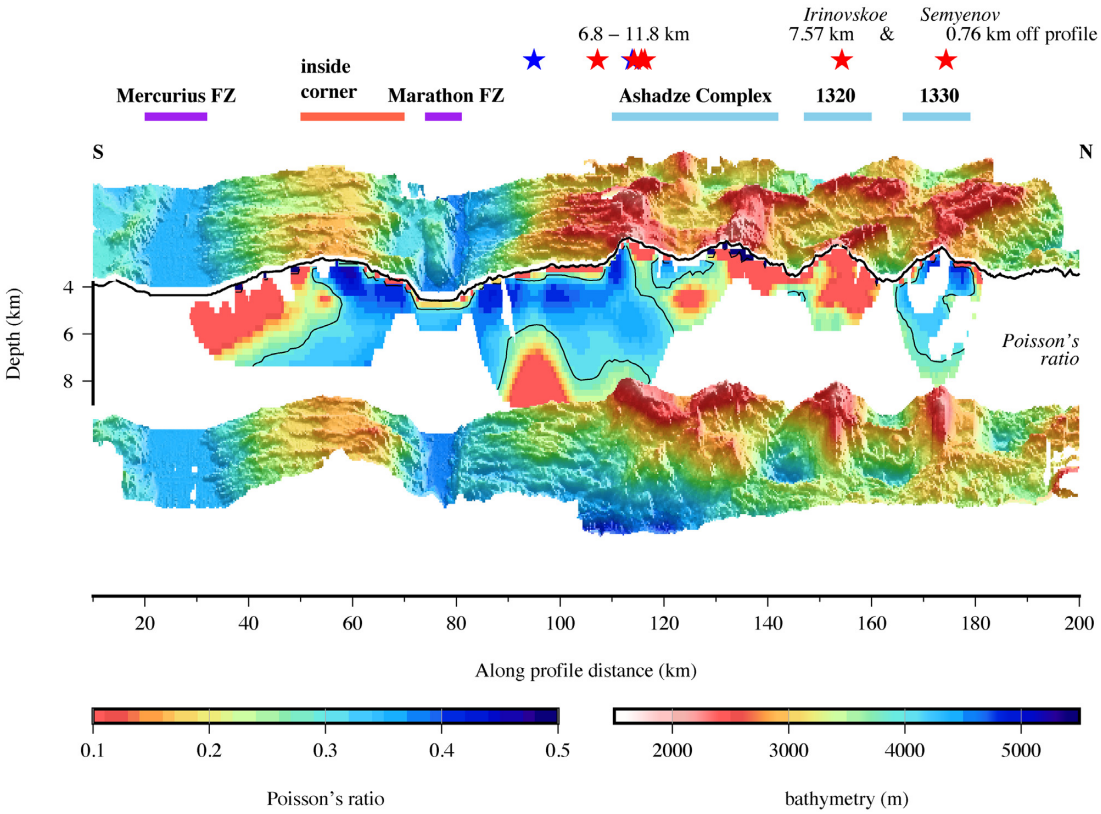

Figure 11. Crustal perspective of adjacent OCCs along Profile R, with the bathymetry sliced along profile location to show the variation in Poisson's ratio beneath each OCC and the Marathon FZ. Prominent topographic features and hydrothermal vents (red star–active; blue star–inactive) are annotated above. The *Poisson's ratio model* is masked to only show areas of ray coverage (*cf.* Fig. 7d).

structure, it extends to a shallower crustal depth than the 1320 OCC to the north. Consequently, the detachment surfaces underlying these OCCs demonstrate varying degrees of lateral slip despite being within ∼1 Myr of the ridge axis (Fig. 1). The correlation between seismic structure and lithology, and seabed morphology is shown in Fig. 11.

Along axis, the variations in velocity and density suggest that each OCC formed separately, such that they are structurally distinct. The boundaries between OCCs are marked by a thinner crust and occur over a zone no more than a few kilometres in width (Fig. 11). The magmatic-like velocity–depth structure and ∼1 km thicker crust of the 1320 OCC, compared to the other OCCs of the western ridge flank, coupled with observations of neovolcanic features on the seabed, the attenuation of seismic arrivals (Simão *et al.* 2016) and magnetic anomaly measurements (Searle *et al.* 2018), suggest that this feature is currently associated with a region of focused magmatism located in the axial region to the east of its hanging-wall cut-off and to its north, and is consistent with Howell *et al.*'s (2019) interpretation that the magmatic accretion-type seabed morphology lying in between the 1320 and 1330 OCCs represents a focus of waxing magma supply, as also suggested by MacLeod *et al.* (2009). Consequently, the magmatic spreading that is occurring between the 1320 and 1330 OCCs, should result in faster fault migration off-axis occurring there, than to the south. Thus, anticlockwise rotation of the 1320 OCC is apparent from the concave to the north and convex to the south geometry of its hanging-wall cut-off currently (Figs 1c and 2d), despite it having ridge perpendicular corrugations on the detachment surface reflecting its past slip direction.

The microseismicity observed in the 6-month period between JC102 and JC109 (Parnell-Turner *et al.* 2017; Fig. 2a) is concentrated to the east of the 1320 OCC (*cf.* Fig. 2d), along the inward-facing fault structure to the north (*cf.* Fig. 2c), and along the southern flank of the 1330 OCC (*cf.* Fig. 2b). These observations suggest that deformation is concentrated in a zone surrounding the ridge axis to the east of the 1320 OCC which, together with magmatic constructions on the seabed, indicates that the 13°N segment may have transitioned from a faulting-dominated period, into a magmatic one in response to a waxing of the magma supply. This magma supply is currently focused between the 1320 and 1330 OCCs. Consequently, the inward-facing faults forming to the north of the 1320 OCC may be linked to it on the basis of the associated microseismicity, but unlinked to the 1330 OCC. The 1320 and 1330 detachments are, therefore, separate features, with the east–west trending pattern of microseismicity demonstrating relative slip between the magmatic zone and the relict 1330 OCC to the north. On the basis of Howell *et al.*'s (2019) modelling, the absence of inward-facing normal faults forming between the 1320 and the northern Ashadze Complex OCCs, suggests that here, a faulting regime ($M < 1$) still predominates.

6.3 Overview

The spreading segment between 12°40′N and 13°40′N is known to be marked by several oceanic core complexes representing plutonic and mantle rocks exhumed by large offset oceanic detachment faults, which suggests that this segment has predominantly been in a phase of amagmatic spreading. In addition to the *P*-wave velocity

structure, the observed *S*-wave velocity structure has revealed the true extent of the along axis variation in lithology. The key results are that the corrugated surfaces of the 1330 OCC and, although less clearly so, the central portion of Ashadze Complex mark the top of regions of serpentinized mantle, whereas the blocky crust of the 1320 OCC (and the blockier, rougher portions of Ashadze) appears entirely magmatic.

Although our results do not contradict the idea that the 1320 and 1330 OCCs are structurally distinct, Profile R crosses different portions of these OCCs and does not fully resolve the region between them to full uppermost mantle depth. More surprisingly, the outside corner crust between the Ashadze Complex and the Marathon FZ to the south, appears to consist of a thin veneer of volcanics above a 2–4 km-thick layer of serpentinites. This is surprising as outside corners are generally thought to be more magmatically robust than inside corners, whereas here the crusts are seismically indistinguishable. The mechanism of mantle exhumation is obscured by the volcanics but may be either by one or two long-lived normal faults (oceanic detachments) or possibly by many cross-cutting detachments operating in a flip-flop manner as described for the ultraslow SWIR (Reston 2018).

Overall, the pattern seems to one of tectonic spreading, unroofing first blocky, rough magmatic crust and then smoother, corrugated mantle serpentinites, punctuated by periods of magmatism. Towards the southern end of the spreading segment, however, spreading appears to have been more continuously magma-poor.

7 CONCLUSIONS

This study of the 13°N segment of the MAR aimed to investigate the crustal structure, lithology and inter-relationships between OCCs, determine any along axis continuity of each OCC's detachment, and better understand the relationship between magmatism and the longevity of OCCs. It also aimed to better understand the relationship with the adjacent segment bounding fracture zones to the south and a change in ridge geometry, mid-segment, to the north. From our study, we draw the following conclusions.

(1) *P-wave* and *S-wave*, V_p/V_s and *Poisson's ratio*, and *density models* collectively show that each OCC along the western flank of the 13°N segment of the MAR has a distinct velocity–depth structure, with the horizontal transition between them occurring over a zone of a few kilometres in width.

(2) Each OCC shows a contrasting *P*-wave and *S*-wave velocity pattern at shallow subseabed depth, and density structures consistent with the *P*-wave velocity.

(3) The V_p/V_s ratio (and equivalent Poisson's ratio) demonstrates the extent of lower crustal and upper mantle exhumation beneath each OCC, with the 1330 and southern Ashadze OCCs having upper-mantle-like lithologies exhumed to shallow subseabed depth, while for the 1320 OCC, the velocity and density models suggest that the upper crust comprises mainly basaltic lithologies despite the reported exposures of gabbros and serpentinites (Escartin *et al.* 2017).

(4) Our combined models favour the localized model of OCC evolution, in which OCCs are spatially restricted, structurally isolated and ephemeral features that are switched on and off by variations between magma-dominated and faulting-dominated ridge axis conditions.

(5) The prominent inward-facing normal faults located north of the 1320 OCC may be linked with the 1320 detachment surface, extending along axis as far north as the southern edge of the 1330 OCC. This region of magmatic accretion-type seabed morphology and normal faulting coincides with the current focus of magmatism between the OCCs as marked by volcanic craters and lava flows on the seabed.

(6) The magmatism and active faulting behind (west of) the footwall breakaway of the 1330 OCC (Peirce *et al.* 2019a) and the microseismicity concentrated in a band along its southern flank (Parnell-Turner *et al.* 2017), suggest a readjustment of ridge geometry along axis is underway, as part of which a transform offset is forming that will ultimately result in a westward ridge jump and accommodate the 1330 OCC in its inside corner on the eastern flank of the ridge axis to the north.

(7) The outside corner to the north of the Marathon FZ has a relatively low *S*-wave velocity within the upper crust corresponding to a region of magmatic accretion-type seabed morphology.

(8) Marathon FZ has a thin crust with low *P*-wave velocity, which is restricted to within its bathymetric footprint. The corresponding low *S*-wave velocity zone extends laterally within the lower crust for at least 20 km beyond the footprint of the FZ, suggesting that transform-fracture zone deformation may not be confined to a narrow region. Such extensive faulting provides pathwdro.dur.ac.ukays for fluid flow that results in extensive metamorphism of the lower crust and serpentinization of the uppermost mantle.

ACKNOWLEDGEMENTS

This research project was funded by the Natural Environment Research Council (NERC) grants NE/J02029X/1, NE/J022551/1 and NE/J021741/1. We would like to thank all involved in the planning and acquisition of data during research cruise JC132 (Reston & Peirce 2016), including the officers, engineers and crew of the RRS James Cook, the scientific party and all seagoing technicians. The NERC Ocean-Bottom Instrumentation Facility (Minshull *et al.* 2005) provided the OBSs used in this project, together with their technical support at sea. The WA data were manipulated for plotting using Seismic Unix. All figures were prepared using the Generic Mapping Tools (GMT) package (Wessel & Smith 1998). All data from cruises JC102, JC109 and JC132 are archived at the NERC's British Oceanographic Data Centre (www.bodc.ac.uk), and the final accepted version of this manuscript is available through Durham Research Online (dro.dur.ac.uk). We thank our three reviewers for their very positive and constructive comments.

REFERENCES

Albers, E., Schroeder, T. & Bach, W., 2019. Melt impregnation of mantle peridotite facilitates high-temperature hydration and mechanical weakening: implications for oceanic detachment faults, *Geochem. Geophys. Geosyst.,* **20**(1), 84–108.

Beltenev, V. *et al.*, 2007. A new hydrothermal field at 13°30′N on the Mid-Atlantic Ridge, *InterRidge News,* **16,** 10–11.

Berge, P.A., Fryer, G.J. & Wilkins, R.H., 1992. Velocity porosity relationships in the upper oceanic-crust—theoretical considerations, *J. geophys. Res.,* **97,** 15 239–15 254.

Blackman, D.K. & Forsyth, D.W., 1991. Isostatic compensation of tectonic features of the Mid-Atlantic Ridge: 25–27°30′S, *J. geophys. Res.,* **96,** 11 741–11 758.

Bonatti, E., 1976. Serpentine protrusions in the oceanic crust, *Earth planet. Sci. Lett.,* **32,** 107–113.

Bonatti, E., 1978. Vertical tectonism in oceanic fracture zones, *Earth planet. Sci. Lett.,* **37,** 369–379.

Bortnikov, N.S., Simonov, V.A., Borovikov, A.A., Bel'tenev, V.E., Amplieva, E., Kotlyarov, A.V. & Bryanskiy, N.V., 2015. The metalliferous fluid of

the hydrothermal sulfide system associated with the oceanic core complex 13°20′N: the Mid-Atlantic Ridge (LA-ICP-MS and fluid inclusions), in *Oceanic Core Complexes and Hydrothermalism, Russian Ridge 2105 Workshop Program*, Moscow, Russia, pp. 80–83.

Bratt, S.R. & Solomon, S.C., 1984. Compressional and shear-wave structure of the East Pacific Rise at 11°20′N – constraints from 3-component ocean bottom seismometer data, *J. geophys. Res.,* **89,** 6095–6110.

Buck, W.R., 1988. Flexural rotation of normal faults, *Tectonics,* **7,** 959–973.

Buck, W.R., 1993. Effect of lithospheric thickness on the formation of high- and low-angle normal faults, *Geology,* **21,** 933–936.

Buck, W.R., Lavier, L.L & Poliakov, A.N.B., 2005. Modes of faulting at mid-ocean ridges, *Nature,* **434,** 719–723.

Bullock, A.D. & Minshull, T.A., 2005. From continental extension to seafloor spreading: crustal structure of the Goban Spur rifted margin, southwest of the UK, *Geophys. J. Int.,* **163,** 527–546.

Calvert, A.J. & Potts, C.G., 1985. Seismic evidence for hydrothermally altered mantle beneath old crust in the Tydeman Fracture-Zone, *Earth planet. Sci. Lett.,* **75**(4), 439–449.

Cann, J.R. *et al.*, 1997. Corrugated slip surfaces formed at ridge-transform intersections on the Mid-Atlantic Ridge, *Nature,* **385,** 329–332.

Cannat, M., Bideau, D. & Hébert, R., 1990. Plastic-deformation and magmatic impregnation in serpentinized rocks from the Garrett Transform-Fault (East Pacific Rise), *Earth planet. Sci. Lett.,* **101**(2–4), 216–232.

Carlson, R.L., 2010. How crack porosity and shape control seismic velocities in the upper oceanic crust: modeling downhole logs from Holes 504B and 1256D, *Geochem. Geophys. Geosyst.,* **11,** doi:10.1029/2009GC002955.

Carlson, R.L., 2014. The effects of alteration and porosity on seismic velocities in oceanic basalts and diabases, *Geochem. Geophys. Geosyst.,* **15**(12), 4589–4598.

Carlson, R.L. & Miller, D.J., 1997. A new assessment of the abundance of serpentinite in the oceanic crust, *Geophys. Res. Lett.,* **24,** 457–460.

Carlson, R.L. & Miller, D.J., 2004. Influence of pressure and mineralogy on seismic velocities in oceanic gabbros: implications for the composition and state of the lower oceanic crust, *J. geophys. Res.,* **109,** doi:10.1029/2003JB002699.

Cherkashov, G. *et al.*, 2008. Two new hydrothermal fields at the Mid-Atlantic Ridge, *Mar. Georesour. Geotechnol.,* **26**(4), 308–316, doi.org/10.1080/10641190802400708.

Cherkashov, G., Lazareva, L. & Stepanova, T., 2010a. Massive sulfide deposits at Semyenov cluster: mineralogy, age and evolution, in *Miner. Ocean Deep Miner. Min, Joint International Meeting*, St. Petersbourg, Russia, pp. 52–57.

Cherkashov, G. *et al.*, 2010b. Seafloor massive sulfides from the northern equatorial Mid-Atlantic Ridge: new discoveries and perspectives, *Mar. Georesour. Geotechnol.,* **28**(3), 222–239, doi.org/10.1080/1064119X.2010.483308.

Cherkashov, G., Kuznetsov, V., Kuksa, K., Tabuns, E., Maksimov, F. & Bel'tenev, V. 2016. Sulfide geochronology along the northern equatorial Mid-Atlantic Ridge, *Ore Geol. Rev.,* doi:10.1016/j.oregeorev.2016.10.015.

Cherkashev, G.A. *et al.*, 2013. Massive sulfide ores of the northern equatorial Mid-Atlantic Ridge, *Oceanology,* **53**(5), 607–619.

Christensen, N.I., 1996. Poisson's ratio and crustal seismology, *J. geophys. Res.,* **101**(B2), 3139–3156.

Christensen, N.I., 2004. Serpentinites, peridotites and seismology, *Int. Geol. Rev.,* **46**(9), 795–816.

Christensen, N.I. & Mooney, W.D., 1995. Seismic velocity structure and composition of the continental-crust—a global view, *J. geophys. Res.,* **100**(B6), 9761–9788.

Christeson, G.L., Purdy, G.M. & Fryer, G.J., 1994. Seismic constraints on shallow crustal emplacement processes at the fast spreading East Pacific Rise, *J. geophys. Res.,* **99**(B9), 17 957–917 973.

Christeson, G.L., Shaw, P.R. & Garmany, J.D., 1997. Shear and compressional wave structure of the East Pacific Rise, 9°–10°N, *J. geophys. Res.,* **102**(B4), 7821–7835.

Collier, J.S. & Singh, S.C., 1998. Poisson's ratio structure of young oceanic crust, *J. geophys. Res.,* **103**(B9), 20 981–20 996.

Collins, J.A., Smith, D.K. & McGuire, JJ., 2012. Seismicity of the Atlantis Massif detachment fault, 30°N at the Mid-Atlantic Ridge, *Geochem. Geophys. Geosyst.,* **13,** Q0AG11, doi:10.1029/2012GC004210.

deMartin, B.J., Sohn, R.A., Canales, J.P. & Humphris, S.E., 2007. Kinematics and geometry of active detachment faulting beneath the Trans-Atlantic Geotraverse (TAG) hydrothermal field on the Mid-Atlantic Ridge, *Geology,* **35**(8), 711–714.

Detrick, R.S & Purdy, G.M., 1980. The crustal structure of the Kane fracture zone from seismic refraction studies, *J. geophys. Res.,* **85**(B7), 3759–3777.

Detrick, R.S., Cormier, M.H., Prince, R.A., Forsyth, D.W. & Ambos, E.L., 1982. Seismic constraints on the crustal structure within the Vema fracture zone, *J. geophys. Res.,* **87**(B13), 599–612.

Detrick, R., White, R. & Purdy, G., 1993. Crustal structure of North Atlantic fracture zones, *Rev. Geophys.,* **31**(4), 439–458.

Dick, H.J.B., Tivey, M.A. & Tucholke, B.E., 2008. Plutonic foundation of a slow-spreading ridge segment: oceanic core complex at Kane megamullion, 23°30′N, 45°20′W, *Geochem. Geophys. Geosyst.,* **9,** Q05014, doi:10.1029/2007GC001645.

Domenico, S.N., 1984. Rock lithology and porosity determination from shear and compressional wave velocity, *Geophysics,* **49**(8), 1188–1195.

Dunn, R.A., Arai, R., Eason, D.E., Canales, J.P. & Sohn, R.A., 2017. Three-dimensional seismic structure of the Mid-Atlantic Ridge: an investigation of tectonic, magmatic, and hydrothermal processes in the Rainbow area, *J. geophys. Res.,* **122,** 9580–9602.

Escartın, J.C., Mevel, C., MacLeod, C.J. & McCaig, A.M., 2003. Constraints on deformation conditions and the origin of oceanic detachments: the Mid-Atlantic ridge core complex at 15°45′N, *Geochem. Geophys. Geosyst.,* **4**(8), doi:10.1029/2001GC000278.

Escartın, J., Smith, D.K., Cann, J., Schouten, H., Langmuir, C.H. & Escrig, S., 2008. Central role of detachment faults in accretion of slow-spreading oceanic lithosphere, *Nature,* **455,** 790–794.

Escartin, J. *et al.*, 2017. Tectonic structure, evolution, and the nature of oceanic core complexes and their detachment fault zones (13°20′N and 13°30′N, Mid Atlantic Ridge), *Geochem. Geophys. Geosyst.,* **18**(4), 1451–1482.

Forsyth, D.W. 1992. Finite extension and low-angle normal faulting, *Geology,* **20**(1), 27–30.

Fowler, C.M.R., 1976. Crustal structure of Mid-Atlantic ridge crest at 37°N, *Geophys. J. R. astr. Soc.,* **47**(3), 459–491.

Gerya, T., 2010. Dynamical instability produces transform faults at mid-ocean ridges, *Science,* **329,** 1047–1050.

Gerya, T.V., 2013. Three-dimensional thermomechanical modeling of oceanic spreading initiation and evolution, *Phys. Earth planet. Inter.,* **214,** 35–42.

Grevemeyer, I., Reston, T. & Möller, S., 2013. Micro-seismicity of oceanic core complexes: the Mid-Atlantic Ridge at 7°S to 8°15′S and at the Logatchev Massif, 14°40′N to 14°50′N, *Geochem. Geophys. Geosyst.,* **14,** 3352–3554.

Grevemeyer, I., Hayman, N.W., Peirce, C., Schwardt, M., Van Avendonk, H.J.A., Dannowski, A. & Papenberg, C., 2018a. Episodic magmatism and serpentinised mantle exhumation at an ultraslow-spreading centre, *Nat. Geosci.,* doi:10.1038/s41561-018-0124-6.

Grevemeyer, I., Ranero, C.R. & Ivandic, M., 2018b. Structure of oceanic crust and serpentinisation at subduction trenches, *Geosphere,* **14**(2), 1–23.

Grevemeyer, I. *et al.*, 2019. Constraining the maximum depth of brittle deformation at slow- and ultraslow-spreading ridges using microseismicity, *Geology,* **47,** doi:10.1130/G46577.1.

Hébert, R., Bideau, D. & Hekinian, R., 1983. Ultramafic and mafic rocks from the Garrett transform-fault near 13°30′S on the East Pacific Rise—igneous petrology, *Earth planet. Sci. Lett.,* **65**(1), 107–125.

Hekinian, R., Bideau, D., Cannat, M., Francheteau, J. & Hébertd, R., 1992. Volcanic activity and crustal mantle exposure in the ultrafast Garrett transform-fault near 13°28S in the Pacific, *Earth planet. Sci. Lett.,* **108**(4), 259–275.

Howell, S.M., Ito, G., Behn, M.D., Martinez, F., Olive, J.-A. & Escartín, J., 2016. Magmatic and tectonic extension at the Chile Ridge: evidence for mantle controls on ridge segmentation, *Geochem. Geophys. Geosyst.,* **17,** 2354–2373.

Howell, S.M., Olive, J.-O., Ito, G., Behn, M.D., Escartin, J. & Klaus, B., 2019. Seafloor expression of oceanic detachment faulting reflects gradients in mid-ocean ridge magma supply, *Earth planet. Sci. Lett.,* **516,** 176–189.

Hudson, J.A., 1980. Overall properties of a cracked solid, *Math. Proc. Camb. Phil. Soc.,* **88**(02), 371–384.

Kim, E., Toomey, D.R., Hooft, E.E.E., Wilcock, W.S.D., Weekly, R.T., Lee, S.-M. & Kim, Y.H., 2018. Upper crustal Vp/Vs ratios at the Endeavour Segment, Juan de Fuca Ridge, from joint inversion of *P* and *S* traveltimes: implications for hydrothermal circulation, *Geochem. Geophys. Geosyst.,* **20,** 208–229, 10.1029/2018GC007921.

Kuo, B.Y. & Forsyth, D.W., 1988. Gravity anomalies of the ridge-transform system in the South Atlantic between 31 and 34.5°S—upwelling centers and variations in crustal thickness, *Mar. Geophys. Res.,* **10**(3-4), 205–232.

Lavier, L.L., Buck, W.R. & Poliakov, A.N., 2000. Factors controlling normal fault offsets in an ideal brittle layer, *J. geophys. Res.,* **105,** 23 431–23 442.

Macdonald, K.C., 1982. Mid-ocean ridges: fine scale tectonic, volcanic and hydrothermal processes within the plate boundary zone, *Annu. Rev. Earth Planet. Sci.,* **10,** 155–190.

MacLeod, C.J. *et al.*, 2002. Direct geological evidence for oceanic detachment faulting: the Mid-Atlantic Ridge, 15°45′N, *Geology,* **30,** 879–882.

MacLeod, C.J., Searle, R.C., Murton, B.J., Casey, J.F., Mallows, C., Unsworth, S.C., Achenbach, K.L. & Harris, M., 2009. Life cycle of oceanic core complexes, *Earth planet. Sci. Lett.,* **287,** 333–344.

MacLeod, C.J., Carlut, J., Escartin, J., Horen, H. & Morris, A., 2011. Quantitative constraint on footwall rotations at the 15°45′N oceanic core complex, Mid-Atlantic Ridge: implications for oceanic detachment fault processes, *Geochem. Geophys. Geosyst.,* **12,** Q0AG03, doi:10.1029/2011GC003503.

Mallows, C. & Searle, R.C., 2012. A geophysical study of oceanic core complexes and surrounding terrane, Mid-Atlantic Ridge at 13°-14°N, *Geochem. Geophys. Geosyst.,* **13,** Q06016, doi:10.1012/2005C004075.

Minshull, T.A., White, R.S., Mutter, J.C., Buhl, P., Detrick, R.S., Williams, C.A. & Morris, E., 1991. Crustal structure at the Blake Spur fracture zone from expanding spread profiles, *J. geophys. Res.,* **96,** 9955–9984.

Minshull, T.A., Sinha, M.C. & Peirce, C., 2005. Multi-disciplinary, subseabed geophysical imaging: a new pool of 28 seafloor instruments in use by the United Kingdom Ocean Bottom Instrument Consortium, *Sea Technol.,* **46,** 27–31.

Minshull, T.A., Müller, M.R. & White, R.S., 2006. Crustal structure of the Southwest Indian Ridge at 66E: seismic constraints, *Geophys. J. Int.,* **166,** 135–147.

Momoh, E., Cannat, M., Watremez, L., Leroy, S. & Singh, S.C., 2017. Quasi-3-D seismic reflection imaging and wide-angle velocity structure of nearly amagmatic oceanic lithosphere at the ultraslow-spreading Southwest Indian Ridge, *J. geophys. Res.,* **122,** 9511–9533.

Moore, D.E., Lockner, D.A., Ma, S.L., Summers, R. & Byerlee, J.D., 1997. Strengths of serpentinite gouges at elevated temperatures, *J. geophys. Res.,* **102**(B7), 14 787–14 801.

Morris, A.R., Gee, J.S., Pressling, N.J., John, B.E., MacLeod, C.J., Grimes, C.B. & Searle, R.C., 2009. Footwall rotation in an oceanic core complex quantified using reorientated Integrated Ocean Drilling Program core samples, *Earth planet. Sci. Lett.,* **287,** 217–228.

Parnell-Turner, R., Sohn, R.A., Peirce, C., Reston, T.J., MacLeod, C.J., Searle, R.C. & Simão, N.M., 2017. Oceanic detachment faults generate compression in extension, *Geology,* **45**(10), 923–926.

Peirce, C., 2014a. The role and detachment of faulting at slow-spreading mid-ocean ridges: RRS James Cook cruise report JC102, Durham University (unpublished), pp. 19, https://www.bodc.ac.uk/resources/inventories/cruise_inventory/reports/jc102.pdf.

Peirce, C., 2014b. The role and detachment of faulting at slow-spreading mid-ocean ridges: RRS James Cook cruise report JC109, Durham University (unpublished), pp. 26, https://www.bodc.ac.uk/resources/inventories/cruise_inventory/reports/jc109.pdf.

Peirce, C., Reveley, G., Robinson, A.H., Funnell, M.J., Searle, R.C., Simão, N.M., MacLeod, C.J. & Reston, T.J., 2019a. Constraints on crustal structure of adjacent OCCs and segment boundaries at 13°N on the Mid-Atlantic Ridge, *Geophys. J. Int.,* **217**(2), 988–1010.

Peirce, C., Robinson, A.H., Campbell, A.M., Funnell, M.J., Grevemeyer, I., Hayman, N.W., Van Avendonk, H.J.A. & Castiello, G., 2019b. Seismic investigation of an active ocean-continent transform margin: the interaction between the Swan Islands Faults Zone and the ultraslow-spreading Mid-Cayman Spreading Centre, *Geophys. J. Int.,* **219,** 159–184.

Pertsev, A.N., Bortnikov, N., Aranovich, L.Y., Vlasov, E.A., Beltenev, V.E., Ivanov, V.N. & Simakin, S., 2009. Peridotite-melt interaction under transitional conditions between the spinel and plagioclase facies beneath the Mid-Atlantic Ridge: insight from peridotites at 13°N, *Petrology,* **17,** 124–137.

Pertsev, A.N., Bortnikov, N.S., Vlasov, E.A., Beltenev, V.E., Dobretsova, I.G. & Ageeva, O.A., 2012. Recent massive sulphide deposits of the Semenov ore district, Mid-Atlantic Ridge, 1331′N: associated rocks of the oceanic core complex and their hydrothermal alteration, *Geol. Ore Deposits,* **54,** 334–346.

Pockalny, R.A., Gente, P. & Buck, R., 1996. Oceanic transverse ridges: a flexural response to fracture-zone-normal extension, *Geology,* **24**(1), 71–74.

Prada, M., Ranero, C.R., Sallares, V., Zitellini, N. & Grevemeyer, I., 2016. Mantle exhumation and sequence of magmatic events in the Magnaghi-Vavilov Basin (Central Tyrrhenian, Italy): new constraints from geological and geophysical observations, *Tectonophysics,* **689,** 133–142.

Pressling, N., Morris, A., John, B.E. & MacLeod, C.J., 2012. The internal structure of an oceanic core complex: an integrated analysis of oriented borehole imagery from IODP Hole U1309D (Atlantis Massif), *Geochem. Geophys. Geosyst.,* **13,** Q04G10, doi:10.1029/2012C004061.

Reston, T.J., 2018. Flipping detachments: The kinematics of ultraslow spreading ridges, *Earth planet. Sci. Lett.,* **503,** 133–157.

Reston, T.J. & McDermott, K.G., 2011. Successive detachment faults and mantle unroofing at magma-poor rifted margins, *Geology,* **39,** 1071–1074.

Reston, T. & Peirce, C., 2016. The role and detachment of faulting at slow-spreading mid-ocean ridges: RRS James Cook cruise report JC132, Durham University (unpublished), pp. 62, https://www.bodc.ac.uk/resources/inventories/cruise_inventory/reports/jc132.pdf.

Reston, T.J. & Pérez Gussinyé, M., 2007. Lithospheric extension from rifting to continental breakup at magma-poor margins: rheology, serpentinization and symmetry, *Int. J. Earth Sci.,* doi:10.1007/s00531-006-0161-z.

Reston, T.J. & Ranero, C.R., 2011. The 3-D geometry of detachment faulting at mid-ocean ridges, *Geochem. Geophys. Geosyst.,* **12,** doi:10.1029/2011GC003666.

Reston, T.J., Weinrebe, W., Grevemeyer, I., Flueh, E.R., Mitchell, N.C., Kirstein, L., Kopp, C. & Kopp, H., 2002. A rifted inside corner massif on the Mid-Atlantic Ridge at 5° S, *Earth planet. Sci. Lett.,* **200,** 255–269.

Roland, E., Lizarralde, D., McGuire, J.J. & Collins, J.A., 2012. Seismic velocity constraints on the material properties that control earthquake behaviour at the Quebrada-Discovery-Gofar transform faults, East Pacific Rise, *J. geophys. Res.,* **117,** B11102, doi:10.1029/2012JB009422.

Sanfilippo, A., Dick, H.J.B., Marschall, H.R., Lissenberg, C.J. & Urann, B., 2019. Emplacement and high-temperature evolution of gabbros of the 16.5°N oceanic core complexes (Mid-Atlantic Ridge): insights into the compositional variability of the lower oceanic crust, *Geochem. Geophys. Geosyst.,* **20**(1), 40–66.

Sauter, D., Cannat, M., Roumejon, S. *et al.*, 2013. Continuous exhumation of mantle-derived rocks at the Southwest Indian Ridge for 11 million years, *Nat. Geosci.,* **6**(4), 314–320.

Schlindwein, V. & Schmid, F., 2016. Mid-ocean-ridge seismicity reveals extreme types of ocean lithosphere, *Nature,* **535,** 276–279.

Searle, R.C. & Laughton, A.S., 1977. Sonar studies of the Mid-Atlantic Ridge crest near Kurchatov fracture zone, *J. geophys. Res.,* **82,** 5313–5328.

Searle, R.C., Tominaga, M., Peirce, C., Reston, T.J. & MacLeod, C.J., 2016. Near-bottom high resolution magnetic observation over and around an active oceanic core complex, MAR 13°N, T33A-2999, in *American Geophysical Union, Fall Meeting*, San Francisco

Searle, R.C., MacLeod, C., Peirce, C. & Reston, T.J., 2018. The Mid-Atlantic Ridge near 13°20′N: high-resolution magnetic and bathymetric imaging, *Geochem. Geophys. Geosyst.,* doi:10.1029/2018GC007940.

Sempéré, J.-C., Lin, J., Brown, H.S., Schouten, H. & Purdy, G.M., 1993. Segmentation and morphotectonic variations along a slow-spreading center: the Mid-Atlantic Ridge (24°00′N-30°40′N), *Mar. Geophys. Res.,* **15,** 153–200.

Severinghaus, J.P. & Macdonald, K.C., 1988. High inside corners at ridge-transform intersections, *Mar. Geophys. Res.,* **9**(4), 353–367.

Shaw, P.R., 1992. Ridge segmentation, faulting and crustal thickness in the Atlantic Ocean, *Nature,* **358,** 491–493, 10.1038/358490a0.

Simão, N.M., Peirce, C., Falder, M., Reston, T.J., MacLeod, C.J. & Searle, R.C., 2016. Velocity structure of the crust at 13°N on the Mid-Atlantic Ridge: implications for crust accretion and oceanic core complex formation, T33A-2997, in *American Geophysical Union, Fall Meeting*, abstract #T33A-2997, San Francisco.

Simão, N.M., Peirce, C., Funnell, M.J., Robinson, A.H., Searle, R.C., MacLeod, C.J. & Reston, T.J., 2020. Three-dimensional *P*-wave velocity structure of oceanic core complexes at 13°N on the Mid-Atlantic Ridge, *Geophys. J. Int.,* forthcoming.

Smith, D.K., Cann, J.R. & Escartin, J., 2006. Widespread active detachment faulting and core complex formation near 13°N on the Mid-Atlantic Ridge, *Nature,* **443,** 440–444.

Smith, D.K., Escartin, J., Schouten, H. & Cann, J.R., 2008. Fault motion and core complex formation: significant processes in seafloor formation at slow-spreading mid-ocean ridges (Mid-Atlantic Ridge, 13°–15°N), *Geochem. Geophys. Geosyst.,* **9,** Q03003, doi:10.1029/2007GC001699.

Spudich, P. & Orcutt, J., 1980. Petrology and porosity of n oceanic crustal site: results from wave form modelling of seismic refraction data, *J. geophys. Res.,* **85**(B3), 1409–1433, doi.org/10.1029/JB085iB03p01409.

Taylor, M.A.J. & Singh, S.C., 2002. Composition and microstructure of magma bodies from effective medium theory, *Geophys. J. Int.,* **149**(1), 15–21, doi.org/10.1046/j.1365-246X.2002.01577.x.

Thibaud, R., Gente, P. & Maia, M., 1998. A systematic analysis of the Mid-Atlantic Ridge morphology between 15N and 40N: constraints on the thermal structure, *J. geophys. Res.,* **103**(B10), 24 233–24 243.

Tréhu, A.M. & Purdy, G.M., 1984. Crustal structure in the Orozo transform zone, *J. geophys. Res.,* **89**(NB3), 1834–1842.

Tucholke, B.E. & Lin, J., 1994. A geological model for the structure of ridge segments in slow spreading ocean crust, *J. geophys. Res.,* **99,** 11 937–11 958.

Tucholke, B.E., Lin, J. & Kleinrock, M., 1998. Megamullions and mullion structure defining oceanic metamorphic core complexes on the Mid-Atlantic Ridge, *J. geophys. Res.,* **103,** 9857–9866, doi.org/10.1029/98JB00167.

Tucholke, B.E., Behn, M.D., Buck, W.R. & Lin, J., 2008. Role of melt supply in oceanic detachment faulting and formation of megamullions, *Geology,* **36,** 455–458, doi.org/10.1130/G24639A.1.

Tuzo Wilson, J., 1965. A new class of faults and their bearing on continental drift, *Nature,* **207,** 343–347, doi.org/10.1038/207343a0.

van Avendonk, H.J.A., Harding, A.J., Orcutt, J.A. & McClain, J.S., 1998. A two-dimensional tomography study of the Clipperton transform fault, *J. geophys. Res.,* **103,** 17 885–17 899, doi.org/10.1029/98JB00904.

van Avendonk, H.J.A., Harding, A.J., Orcutt, J.A. & McClain, J.S., 2001. Contrast in crustal structure across the Clipperton transform fault from travel time tomography, *J. geophys. Res.,* **106**(B6), 10 961–10 981, doi.org/10.1029/2000JB900459.

Vera, E.E., Mutter, J.C., Buhl, P., Orcutt, J.A., Harding, A.J., Kappus, M.E., Detrick, R.S. & Brocher, T.M., 1990. The structure of 0-My to 0.2-My old oceanic crust at 9N on the East Pacific Rise from expanded spread profiles, *J. geophys. Res.,* **95**(B10), 15 529–15 556, doi.org/10.1029/JB095iB10p15529.

Walsh, J.B., 1968. Attenuation in partially melted material, *J. geophys. Res.,* **73**(6), 2209–2216, doi.org/10.1029/JB073i006p02209.

Walsh, J.B., 1969. New analysis of attenuation in partially melted rock, *J. geophys. Res.,* **74**(17), 4333–4337.

Wessel, P. & Smith, W., 1998. New, improved version of Generic Mapping Tools released, *EOS, Trans. Am. geophys. Un.,* **79,** 579.

White, R.S., Detrick, R.S., Sinha, M.C. & Cormier, M.H., 1984. Anomalous seismic crustal structure of oceanic fracture zones, *Geophys. J. R. astr. Soc.,* **79**(3), 779–798, doi.org/10.1111/j.1365-246X.1984.tb02868.x.

White, R.S., Mckenzie, D. & O'Nions, R.K., 1992. Oceanic crustal thickness from seismic measurements and rare earth element inversions, *J. geophys. Res.,* **97,** 683–715.

Wilson, S.C., Murton, B.J. & Taylor, R.N., 2013. Mantle composition controls the development of an oceanic core complex, *Geochem. Geophys. Geosyst.,* **14,** 1–18, doi.org/10.1002/ggge.20046.

Zelt, C.A., 1998. Lateral velocity resolution from three-dimensional seismic refraction data, *Geophys. J. Int.,* **135,** 1101–1112, doi.org/10.1046/j.1365-246X.1998.00695.x.

Zelt, C.A. & Barton, P.J., 1998. Three-dimensional seismic refraction tomography: a comparison of two methods applied to data from the Faeroe Basin, *J. geophys. Res.,* **103,** 7187–7210, doi.org/10.1029/97JB03536.